New Capabilities and Improvements to the High-Order Glenn Flux Reconstruction Code

Seth C. Spiegel,* Dennis A. Yoder,† James R. DeBonis,† H. T. Huynh,*
Gregory S. Heinlein,‡ Michael R. Borghi Jr.,§ and Nicholas J. Georgiadis†
NASA Glenn Research Center, Cleveland, OH, 44135, USA

The Glenn Flux Reconstruction (GFR) code is a computational fluid dynamics (CFD) code under development at NASA Glenn Research Center. GFR is based on the high-order flux reconstruction (FR) method and provides a large-eddy simulation (LES) capability that is both accurate and efficient for complex aeropropulsion flows. Three significant new capabilities have been added to the code that improve its performance and functionality. First, a variety of explicit Runge-Kutta methods, including some with adaptive time stepping, were added to GFR with two methods offering a 33% improvement in time-to-solution. Second, GFR can now utilize fully unstructured, mixed-element meshes to more easily facilitate the grid generation process for complex geometries. Finally, a rotating reference frame capability has been added to GFR for solving rotating turbomachinery problems. A selection of results demonstrating these new capabilities are presented in this work. The Taylor-Green vortex problem is used to verify the new unstructured capability by showing similar accuracy and resolution for all element types. LES of the Turbulent Heat Flux Phase III (THX3) experiment with comparison to another high-order LES code and a popular Reynolds-averaged Navier-Stokes (RANS) code demonstrates the accuracy of the code for complex aeropropulsion flows. Finally, LES of a spacecraft cabin ventilation fan shows the ability of GFR to efficiently establish a fan performance map and identify operating points for further analysis at high orders of accuracy.

I. Introduction

Computational fluid dynamics (CFD) is now used routinely in aerospace research and development efforts, as continual advances in computing power are allowing for more complex problems to be investigated than previously possible. Additionally, advanced mesh generation techniques for unstructured grid solution procedures have evolved to expedite the creation of meshes for complex configurations starting from computer-aided design (CAD) geometry models. It is now commonplace to be able to generate computational meshes of full aircraft configurations using unstructured grid methods in a fraction of the time than was possible a decade or two ago.

Most aerospace CFD problems involve calculation of turbulent flow, where the accuracy of simulations is determined by the choice of turbulent flow calculation approach. The established state-of-practice for aerospace problems is the Reynolds-averaged Navier-Stokes (RANS) method, where all of the turbulent effects are replaced with a model. It is recognized that limitations inherent to the RANS method prohibit the accurate simulation of challenging three-dimensional boundary layers with flow separation, shock-boundary layer interactions, free-shear layer mixing (i.e., coflowing jets), compressibility, and temperature effects; all of which are flow features found in modern aerospace systems and their components.[1] Propulsion system (i.e., air-breathing and rocket engine) simulations frequently require consideration of all of these flow physics,[2] in addition to chemical reactions in the combustor where turbulence-chemistry interaction remains an exceptionally difficult computational challenge.

*Aerospace Engineer, Inlets and Nozzles Branch, AIAA Member.
†Aerospace Engineer, Inlets and Nozzles Branch, AIAA Associate Fellow.
‡Aerospace Engineer, Multiscale & Multiphysics Modeling Branch, AIAA Member.
§Aerospace Engineer, Turbomachinery and Turboelectric Systems Branch, AIAA Member.

In order to address the inadequacies of RANS methods for these challenging turbulent flow physics, scale-resolving simulations (SRS) have been explored and adopted in more engineering CFD applications in recent years.[3] Direct numerical simulation (DNS) remains a tool only practical for simple geometries at low Reynolds numbers. Large-eddy simulation (LES) is now being employed for select flows beyond simple canonical cases. Wall-resolved LES (WRLES) is still very expensive as nearly all of the relevant turbulent scales are directly calculated and only the sub-grid stresses are modeled. Alternative SRS methods, such as hybrid RANS-LES (HRLES) and wall-modeled LES (WMLES) are now being employed, and have provided accuracy improvements over RANS in some cases for post-separation aerodynamic prediction. The greatest success has been for problems where the flow separation is due to some geometric feature and is not highly dependent on incoming boundary layer state. Both of these methods treat near-wall regions with much less costly, but inherently less physics-based, compromises to calculating the near-wall turbulence energy spectrum. For pre-separation aerodynamics, HRLES and WMLES do not offer any real improvements beyond RANS methods. Improvement in the accuracy of separated flow field prediction including the regions of onset to separation will likely only be realized with WRLES (or DNS which will remain limited in applicability relative to WRLES in the foreseeable future due to computational cost).

HRLES and WMLES have demonstrated some success for calculations of geometrically-induced separated flows using low-dissipation second-order accurate numerical schemes. In contrast to its less computationally expensive cousins, a distinguishing feature of WRLES is the potential for greater solution fidelity across a broader range of turbulent flow problems. However, the spatial and temporal resolution needed for WRLES requires high-order (higher than second) numerical schemes historically only found in structured grid methods with large stencils. Structured methods have numerous drawbacks: difficulty in grid generation, high sensitivity to grid quality, complex boundary conditions, and poor scalability for parallel computing. These drawbacks severely limit the ability of these codes to compute complex aeropropulsion configurations, e.g., noise suppressing nozzles.[4] High-order methods with large stencils also pose a challenge to implementation in unstructured CFD tools based on traditional second-order finite-volume methods, where it is all but impossible to apply these stencils on grids containing arbitrary cell shapes. The past few decades have seen rapidly expanding interest in using high-order finite-element/spectral-element methods for aerospace applications. Spectral element methods are able to achieve high-order accuracy in arbitrarily shaped elements by using a finite series expansion (e.g., Taylor or Fourier series) to create a high-order function within each cell. Particular interest has been focused on using discontinuous Galerkin (DG)[5–7] and flux reconstruction (FR)[8–11] methods for unstructured grid analyses, with various research groups showing successful use of FR in LES solvers intended for aerospace applications.[12–19]

This paper describes the continuing work to develop a high-order WRLES code using the FR methods for aerospace applications, with a focus on propulsion problems. This work builds upon previous efforts, described in Ref. 20, to develop a baseline flow solver known as the Glenn Flux Reconstruction (GFR) code. Since that initial publication, a number of enhancements have been made to GFR to enable WRLES calculations of challenging turbulent flows. This paper describes three significant enhancements: the addition of new explicit Runge-Kutta methods that reduce the overall time-to-solution of a simulation by up to 33%; implementation of the FR method for unstructured mixed-element meshes; and a rotating reference frame for simulation of turbomachinery components such as fans, compressors, and turbines. Finally, demonstration of the enhancements for configurations of varying complexity are used for verification and validation of these new capabilities in GFR.

II. Code Description

The Glenn Flux Reconstruction (GFR) code is a CFD code under development at NASA Glenn Research Center. GFR is based on the high-order FR method and provides an LES capability that is both accurate and efficient for complex aeropropulsion flows. The accuracy of a GFR simulation is generally $\mathcal{P}+1$ for nonlinear equations such as the Euler or Navier-Stokes equations,[20,21] where $\mathcal{P}$ is the degree of the solution polynomial used by the FR method to approximate the high-order solution within each cell. GFR currently does not employ any explicit modeling for the unresolved sub-grid scale turbulence; therefore, all simulations utilize the implicit LES method where the numerical dissipation present in the solution is assumed to act as a sub-grid scale model. Further details regarding the numerical methods and existing capabilities in GFR can be found in Ref. 18 and 20. The remainder of this section covers three significant new capabilities that have been added to the code to improve its performance and functionality towards accurate and efficient

Algorithm 1 Low storage implementation (3S*)

$S_1 \leftarrow u^n; S_2 \leftarrow 0; S_3 \leftarrow u^n$
for $i = 1 : s$ **do**
  $\tau \leftarrow t^n + c_i \Delta t$
  $S_2 \leftarrow S_2 + \delta_i S_1$
  $S_1 \leftarrow \gamma_{1,i} S_1 + \gamma_{2,i} S_2 + \gamma_{3,i} S_3 + \beta_i \Delta t \mathbf{R}(\tau, S_1)$
end for
$u^{n+1} \leftarrow S_1$

Algorithm 2 Embedded-pair low storage implementation (3S*$_+$)

$S_1 \leftarrow u^n; S_2 \leftarrow 0; S_3 \leftarrow u^n; S_4 \leftarrow u^n$
for $i = 1 : s$ **do**
  $\tau \leftarrow t^n + c_i \Delta t$
  $S_2 \leftarrow S_2 + \delta_i S_1$
  $R_i \leftarrow \mathbf{R}(\tau, S_1)$
  $S_1 \leftarrow \gamma_{1,i} S_1 + \gamma_{2,i} S_2 + \gamma_{3,i} S_3 + \beta_i \Delta t R_i$
  $S_4 \leftarrow S_4 + \hat{b}_i \Delta t R_i$
end for
$u^{n+1} \leftarrow S_1$
$\hat{u}^{n+1} \leftarrow S_4$
if $\hat{b}_{s+1} \neq 0$ **then**
  $\hat{u}^{n+1} \leftarrow \hat{u}^{n+1} + \hat{b}_{s+1} \Delta t \mathbf{R}\left(t^{n+1}, u^{n+1}\right)$
end if

LES. First, Section II.A details the addition of numerous new explicit Runge-Kutta methods with the goal of reducing the amount of walltime required to obtain a final solution. Next, Section II.B briefly details the new unstructured mixed-element capability. Finally, Section II.C discusses the modifications to the governing Navier-Stokes equations to add a rotating reference frame capability for solving rotating turbomachinery problems.

II.A. Advanced Explicit Runge-Kutta Time Integration Methods

Nearly all previous simulations performed with GFR used the 3-stage/3$^{\text{rd}}$-order Strong Stability Preserving (SSP) Runge-Kutta (SSPRK) scheme,[22] which will be referred to as SSP3. Other explicit Runge-Kutta (ERK) methods previously implemented within GFR include the 1$^{\text{st}}$-4$^{\text{th}}$ order Classic Runge-Kutta methods, 2-stage/2$^{\text{nd}}$-order SSPRK,[22] 5-stage/4$^{\text{th}}$-order SSPRK,[23] and the Carpenter-Kennedy low-storage 5-stage/4$^{\text{th}}$-order ERK methods.[24] In an effort to improve simulation performance in terms of time-to-solution, numerous optimized and embedded-pair ERK methods were added to GFR for evaluation.

The first set of new ERK methods added to GFR are from the work of Al Jahdali et al.,[25] who present a new family of methods that have been optimized for wave propagation problems. These optimized ERK (OERK) methods use the eigenvalues of the discrete spatial operator[25] for the advection equation and isentropic vortex problem to optimize the stability region of each method within the family. Six different schemes were added: 5-stage/3$^{\text{rd}}$-order, 11-stage/3$^{\text{rd}}$-order, 6-stage/4$^{\text{th}}$-order, 15-stage/4$^{\text{th}}$-order, 8-stage/5$^{\text{th}}$-order, and 16-stage/5$^{\text{th}}$-order. Each of these individual schemes has two sets of coefficients, one set optimized using the advection equation and one set optimized using the isentropic vortex problem. Therefore, a total of twelve OERK schemes have been added to GFR: six advection optimized (AOERK) schemes and six vortex optimized (VOERK) schemes. These OERK methods have been implemented using a low-storage algorithm that requires three registers per stage (3S*);[26] the low-storage 3S* algorithm for s stages is shown in Algorithm 1. The function $\mathbf{R}(t^n, u^n)$ represents the evaluation of the right-hand-side residual of the system of equations, where t^n and u^n are respectively the time and solution at time step n, and Δt is the change in time for the current time step. The low-storage 3S* coefficients $[\gamma_{1,i},\ \gamma_{2,i},\ \gamma_{3,i},\ \delta_i,\ \beta_i,\ c_i]$ for all twelve of these OERK schemes can be found in the supplementary material of Ref. 25.

The second set of new ERK methods added to GFR all fit within the family of embedded-pair explicit Runge-Kutta (EPERK) methods. EPERK methods contain an additional Runge-Kutta method of lower order than the primary method that is simultaneously evaluated with minimal additional cost, thus an embedded pair of methods. At the end of a given time step, the difference between these two methods can be viewed as the error in the primary time-stepping method. This error can be used as the input to a PID controller to automate the selection of an optimal time step size for the following iteration.[27–29]

A total of eight EPERK schemes were added to GFR. The first method is the Dormand-Prince[30] 7-stage/5$^{\text{th}}$-order method with an embedded 4$^{\text{th}}$-order scheme. The second method is based off the Dormand-Prince[31] 13-stage/8$^{\text{th}}$-order method with an embedded 7$^{\text{th}}$-order scheme which was modified by Hairer and Wanner[32] to instead use an embedded 5$^{\text{th}}$-order scheme with a 3$^{\text{rd}}$-order correction. The remaining six

Table 1: Performance comparison between new and existing Runge-Kutta methods in GFR.

Runge-Kutta Method	Stages	Scaled $\Delta t/\Delta t_{\text{SSP3}}$	# iterations to $t^* = 20$	Walltime (s) to $t^* = 20$	Speedup vs. SSP3
SSP3[†]	3	1.000	11753	1187	1.00
[#]SSP 5/4[†]	5	1.889	5919	974	1.22
Carpenter-Kennedy 5/4[†]	5	1.556	7186	1201	0.99
VOERK 5/3	5	1.667	6708	1097	1.08
[#]VOERK 11/3	11	4.444	2519	894	1.33
VOERK 6/4	6	1.889	5919	1165	1.02
[#]VOERK 15/4	15	6.000	1866	894	1.33
VOERK 8/5	8	2.556	4376	1133	1.05
VOERK 16/5	16	5.833	1920	1002	1.18
AOERK 16/5	16	5.000	2240	1211	0.98
Dormand-Prince 7/5(4)	7	1.222	9117	1842	0.64
Dormand-Prince 13/8(5)	13	2.378	4726	1934	0.61
OEPERK 5/3(2) FSAL	5	1.767	6116	1090	1.09
[#]OEPERK 9/4(3) FSAL	9	3.333	3193	969	1.22
OEPERK 10/5(4) FSAL	10	2.778	4027	1394	0.85

[†] Already existing in GFR

[#] Method with greater than 20% speedup over baseline SSP3

schemes are two different versions of three optimized EPERK (OEPERK) methods from Ranocha et al.[29] Specifically, the optimized EPERK methods added to GFR from this work include a 5-stage/3$^{\text{rd}}$-order method with an embedded 2$^{\text{nd}}$-order scheme, a 9-stage/4$^{\text{th}}$-order method with an embedded 3$^{\text{rd}}$-order scheme, and a 10-stage/5$^{\text{th}}$-order method with an embedded 4$^{\text{th}}$-order scheme. Each of these optimized methods contains two versions, a base version and a first-same-as-last (FSAL) version. In FSAL methods, the last evaluation of the right-hand-side function needed by the embedded scheme is equivalent to the right-hand-side function needed for the first stage of the following time step. Therefore, this redundancy in FSAL methods can be exploited to reduce the number of right-hand-side evaluations per time step by one.

The implementation and usage of the optimized EPERK schemes follows Ref. 29, starting with the low-storage algorithm shown in Algorithm 2. The quantity $\hat{u}^{n+1}$ represents the solution as updated by the embedded lower-order scheme using the additional coefficients $\hat{b}_i$. The time stepping error from the embedded RK pair is given by

$$\varepsilon_{n+1} = \frac{1}{w_{n+1}}, \quad w_{n+1} = \frac{1}{m}\sum_{i=1}^{m}\left(\frac{u_i^{n+1} - \hat{u}_i^{n+1}}{\texttt{atol} + \texttt{rtol}\cdot\max\left\{\left|u_i^{n+1}\right|, \left|\hat{u}_i^{n+1}\right|\right\}}\right) \tag{1}$$

where m is the total degrees-of-freedom, and `atol` and `rtol` are the respective absolute and relative error tolerances. Finally, the time stepping error is used with a PID controller to determine the time step size for the next iteration

$$\Delta t^{n+1} = \varepsilon_{n+1}^{\beta_1/k}\varepsilon_n^{\beta_2/k}\varepsilon_{n-1}^{\beta_3/k}\Delta t^n \tag{2}$$

where k is the order of the EPERK method, and β_i are the controller parameters. The error tolerances and controller parameters used in this work are those recommended in Ref. 29.

Table 1 shows a performance comparison between the new and existing ERK methods in GFR. Each case was run on the Taylor-Green vortex problem[33–35] with the only difference between each case being the time stepping method used. SSP3 has been the primary method used for all previous GFR simulations, so it is treated as the baseline method for comparisons. The Dormand-Prince and OEPERK methods used a CFL-based time step to ensure that the largest stable time step size was used with each method. The three non-FSAL OEPERK methods are not shown since the performance of those methods was nearly the same as

their FSAL counterparts. All of the advection-optimized ERK methods performed significantly worse than their vortex-optimized counterparts; only the 16-stage/5$^{\text{th}}$-order method is shown to illustrate this point.

Four methods stand out from the results in Table 1. The pre-existing 5-stage/4$^{\text{th}}$-order SSPRK method is 22% faster than the SSP3 method. This method has existed in GFR since the beginning but had not been rigorously explored until this work. The new vortex-optimized 11-stage/3$^{\text{rd}}$-order and 15-stage/4$^{\text{th}}$-order methods both show a speedup of 33% compared to SSP3; the VOERK 11/3 method has since become the default time-stepping method in GFR. The optimized 9-stage/4$^{\text{th}}$-order EPERK method with embedded 3$^{\text{rd}}$-order scheme performs the best out of the EPERK methods at 22% faster than the SSP3 method.

II.B. Unstructured /Mixed-Element Mesh Capability

A full three-dimensional unstructured mixed-element mesh capability has been added to GFR. Previous results[18–21,36] using GFR required a grid containing only structured-type elements, i.e., quadrilaterals and hexahedral elements. Whereas structured-type elements are both more accurate and efficient for high-order FR/DG methods compared to unstructured elements, structured grid generation is significantly more difficult and time consuming for complex geometries. Therefore, this new mixed-element capability enables an expedited CFD workflow—CAD to post-processed solution—for complex geometries.

It has been shown[36–41] that the choice in solution points for a given element type can have a significant effect on the accuracy and stability of the flux reconstruction method. Nodal point sets for structured elements are quite straight forward, with spectral element methods generally utilizing a tensor product of the one-dimensional Legendre-Gauss or Legendre-Gauss-Lobatto quadrature points, with the former being more accurate.[36,38] Conversely, finding optimal nodal point sets for unstructured elements has been an active area of research for decades.[42–48] Recent research[40] has utilized optimization algorithms with increasing computational resources to find sets of quadrature points optimized for various specific properties, e.g., highest accuracy for a given number of points or fewest points for a given accuracy.

The following quadrature rules for unstructured elements have been added to GFR: triangle elements up to $\mathcal{P}8$ using quadrature rules created by Williams;[49] tetrahedra elements up to $\mathcal{P}6$ using quadrature rules created by Shunn and Ham;[50] the quadrature rules for prism elements are a tensor product of triangle and one-dimensional Gauss quadrature, thus limited by the triangle quadrature to $\mathcal{P}8$; and finally, the quadrature rules for pyramid elements are created using a tensor product of hierarchical quadrature rules for quadrilateral elements and a one-dimensional Gauss quadrature.

II.C. Rotating Reference Frame Capability

There are various methods to solving the equations governing rotating turbomachinery fluid flows. These methods primarily fall into two categories: active and passive rotation. Active rotation is akin to a moving grid method where each individual grid component has a specified velocity thus moving the grid within a fixed inertial reference frame; e.g., standing on the ground watching a fan spin. Passive rotation reformulates the equations within a non-inertial reference frame with motion relative to the fixed inertial reference frame; e.g., standing on a fan blade watching everything else spin around you as you rotate with the blade.

Moving grid methods give rise to temporal grid metric terms when transforming the governing equations from physical to computational space. For high-order FR/DG methods, grid geometries are regularly defined by polynomials to accurately define geometry curvature. This means the metric terms are also polynomials, and treatment of these terms requires significant attention to detail when formulating the grid metrics to ensure conservation, accuracy, and stability.[51] Therefore, active rotation is really only a good option to use for rotating turbomachinery flows when a code already has a moving grid capability. On the other hand, passive rotation, more often referred to as a rotating reference frame, is a commonly used method for solving rotating turbomachinery flows[52–55] due to its simplicity and computational efficiency.[53,54]

The Navier-Stokes equations in differential form for a fixed inertial reference frame are

$$\frac{\partial \boldsymbol{Q}}{\partial t} + \frac{\partial}{\partial x}\left[\boldsymbol{F}_I - \boldsymbol{F}_V\right] + \frac{\partial}{\partial y}\left[\boldsymbol{G}_I - \boldsymbol{G}_V\right] + \frac{\partial}{\partial z}\left[\boldsymbol{H}_I - \boldsymbol{H}_V\right] = 0 \tag{3}$$

where $\boldsymbol{Q}$ is the vector of conserved variables

$$\boldsymbol{Q} = \begin{bmatrix} \rho \\ \rho u \\ \rho v \\ \rho w \\ \rho e_o \end{bmatrix} \tag{4}$$

where ρ, $\vec{u} = [u, v, w]$, and e_0 respectively refer to the density, velocity vector, and the total energy per unit mass of the system. $\boldsymbol{F}_I$, $\boldsymbol{G}_I$, and $\boldsymbol{H}_I$ are the inviscid flux vectors in each Cartesian direction given by

$$\boldsymbol{F}_I = \begin{bmatrix} \rho u \\ \rho u u + p \\ \rho u v \\ \rho u w \\ u\left(\rho e_o + p\right) \end{bmatrix} \quad \boldsymbol{G}_I = \begin{bmatrix} \rho v \\ \rho v u \\ \rho v v + p \\ \rho v w \\ v\left(\rho e_o + p\right) \end{bmatrix} \quad \boldsymbol{H}_I = \begin{bmatrix} \rho w \\ \rho w u \\ \rho w v \\ \rho w w + p \\ w\left(\rho e_o + p\right) \end{bmatrix} \tag{5}$$

where p is the static pressure. $\boldsymbol{F}_V$, $\boldsymbol{G}_V$, and $\boldsymbol{H}_V$ are the viscous flux vectors given by

$$\boldsymbol{F}_V = \begin{bmatrix} 0 \\ \tau_{xx} \\ \tau_{xy} \\ \tau_{xz} \\ u\tau_{xx} + v\tau_{xy} + w\tau_{xz} - q_x \end{bmatrix} \quad \boldsymbol{G}_V = \begin{bmatrix} 0 \\ \tau_{yx} \\ \tau_{yy} \\ \tau_{yz} \\ u\tau_{yx} + v\tau_{yy} + w\tau_{yz} - q_y \end{bmatrix} \quad \boldsymbol{H}_V = \begin{bmatrix} 0 \\ \tau_{zx} \\ \tau_{zy} \\ \tau_{zz} \\ u\tau_{zx} + v\tau_{zy} + w\tau_{zz} - q_z \end{bmatrix} \tag{6}$$

where τ_{ij} is the viscous stress tensor and q_i is the heat flux vector.

Thermodynamic closure for Eq. (3) is found through the total energy equation

$$\rho e_0 = \frac{p}{\gamma - 1} + \tfrac{1}{2}\rho u_i u_i \tag{7}$$

where γ is the ratio of specific heats for the fluid in question. The viscous stress tensor, τ_{ij}, is based on Stokes' hypothesis and given by the equation

$$\tau_{ij} = \mu\left(\frac{\partial u_i}{\partial x_j} + \frac{\partial u_j}{\partial x_i} - \frac{2}{3}\frac{\partial u_k}{\partial x_k}\delta_{ij}\right) \tag{8}$$

Above, μ is the molecular viscosity and its relation to the temperature of the fluid, T, is modeled by Sutherland's law

$$\mu = \mu_0\left(\frac{T}{T_0}\right)^{\frac{3}{2}}\frac{T_0 + T_{\text{Suth}}}{T + T_{\text{Suth}}} \tag{9}$$

where μ_0 is the reference viscosity at the reference temperature T_0 and $T_{\text{Suth}} = 110.4\,\text{K}$. The heat flux vector, q_j, is modeled by Fourier's law

$$q_j = -k\frac{\partial T}{\partial x_j} \tag{10}$$

where k is the thermal conductivity which is related to the specific heat at constant pressure, c_p, and Prandtl number, Pr, through the relation

$$k = \frac{c_p \mu}{\text{Pr}} \tag{11}$$

Additionally, with the specific gas constant denoted as R_{gas}, the temperature, pressure, and density of the fluid are related through the ideal gas law

$$p = \rho R_{\text{gas}} T \tag{12}$$

In the present work, the fluid is assumed to be calorically perfect air with the following quantities held constant: the Prandtl number is $\text{Pr} = 0.72$, the ratio of specific heats is $\gamma = 1.4$, and the dimensionalized specific gas constant is $R_{\text{gas}} = 287.15\,\text{J/(kg K)}$.

Let the rotation vector $\vec{\Omega} = [\Omega_x, \Omega_y, \Omega_z]$ give the rotation rate about each of the respective Cartesian axes for a non-inertial reference frame relative to the inertial reference frame. The *absolute* velocity, $\vec{u}$, is equal to the *relative* velocity, $\hat{u}$, in the rotating reference frame plus the rotational velocity, $\vec{\omega} = \vec{\Omega} \times \vec{x}$, of the rotating reference frame, where $\vec{x}$ is the distance vector to the center of rotation:

$$\vec{u} = \hat{u} + \vec{\omega} = \hat{u} + \vec{\Omega} \times \vec{x} \tag{13}$$

The Navier-Stokes equations for a non-inertial rotating reference frame written in terms of the rotating coordinates and absolute velocity is nearly identical to Eq. (3) but with the addition of three new flux terms and a source term:

$$\frac{\partial \boldsymbol{Q}}{\partial t} + \frac{\partial}{\partial x}\left[\boldsymbol{F}_I - \boldsymbol{F}_V - \boldsymbol{F}_R\right] + \frac{\partial}{\partial y}\left[\boldsymbol{G}_I - \boldsymbol{G}_V - \boldsymbol{G}_R\right] + \frac{\partial}{\partial z}\left[\boldsymbol{H}_I - \boldsymbol{H}_V - \boldsymbol{H}_R\right] = \boldsymbol{S}_R \tag{14}$$

The rotation flux terms $\boldsymbol{F}_R$, $\boldsymbol{G}_R$, and $\boldsymbol{H}_R$ are given by

$$\boldsymbol{F}_R = \omega_x \boldsymbol{Q} \quad \boldsymbol{G}_R = \omega_y \boldsymbol{Q} \quad \boldsymbol{H}_R = \omega_z \boldsymbol{Q} \tag{15}$$

and the source term due to inertial forces is given by

$$\boldsymbol{S}_R = \begin{bmatrix} 0 \\ -\rho\Psi_x \\ -\rho\Psi_y \\ -\rho\Psi_z \\ 0 \end{bmatrix} \tag{16}$$

where Ψ_i is defined as $\vec{\Psi} = \vec{\Omega} \times \vec{u}$.

The addition of the rotating flux vectors changes the eigenvalues of the system of equations, so care needs to be taken to account for this when adding a rotating reference frame capability to an existing fixed reference frame CFD code. Fortunately, this change can be easily computed by simply using the rotating velocity in place of the absolute velocity when evaluating the eigenvalues. This ultimately amounts to subtracting out the velocity of the rotating reference frame from the fixed frame eigenvalues, or

$$\hat{\lambda}_{ij} = \lambda_{ij} - \omega_j \tag{17}$$

where λ_{ij} is the eigenvalue of fixed frame equation i in direction j, and $\hat{\lambda}$ is the corresponding eigenvalue for the rotating reference frame equation.

III. Numerical Results

III.A. Verification of Unstructured Capability using Taylor-Green Vortex

The Taylor-Green vortex problem[33] was used to verify the unstructured capability in GFR. This test problem allows for quick and easy testing of different grid topologies due to its simple geometry and setup. Further details of the Taylor-Green vortex problem can be found in Ref. 20, 33–35, 56.

Five families of grids were created for these cases; one for each type of element. The first set consists of a set of tetrahedra-only grids generated in Cadence Fidelity Pointwise with a simple isotropic volume mesh generation; the gray block in Fig. 1 was created using this method. The second set consists of hexahedra-only grids with uniform spacing in all directions. The third set consists of pyramid-only grids which were created by taking a hexahedra-only grid and converting each element into six equal pyramid elements by adding a new grid node in the center of the hexahedral element which serves as the peak vertex point for all six pyramids. The fourth set consists of prism-only grids generated in Pointwise by creating a square two-dimensional domain split into isotropic triangle elements and extruding the surface in the third dimension to create a cube domain; the green blocks in Fig. 1 were created in this manner. Finally, the last set of grids was created to contain all four element types and therefore serve as a final test of the new unstructured mixed-element mesh capability. The cubic domain was split into octants, with each individual octant containing a different grid topology. Figure 1 shows an example of one of these grids which has been exploded to show

the surface grids of each octant. The red block contains only hexahedra cells, the green blocks contain only prism cells, the gray block contains only tetrahedra cells, and the blue blocks contain a mixture of tetrahedra and pyramid cells.

The Taylor-Green vortex problem[33] defines a rich set of data that can be used to analyze the numerical dissipation of a method. Additionally, the solution found by a pseudo-spectral code[34] using 512^3 degrees of freedom (DoF) is available as a reference solution. For the purposes of this work, however, only a brief qualitative comparison of the results across the different sets of grids will be made with the sole intent of verifying that each unstructured element type appears to be working correctly.

The first qualitative comparison shown in Fig. 2 the kinetic energy dissipation rate (KEDR) across the different grids. Figure 2a shows the KEDR for each type of grid using a $\mathcal{P}3$ solution with approximately 64^3 DoF. Even though there is a noticeable difference from the reference solution, the fact that the KEDR trends across all five grids are quite similar indicates the new unstructured capability is working correctly for each of the element types. Figure 2b also shows the KEDR for the different grid types, but instead using $\mathcal{P}4$ solutions with approximately 128^3 DoF. These solutions align very nicely with the reference solution, with the result from the pyramid grid being the only outlier. This particular case required some very minor filtering to keep the solution stable, and this additional dissipation is likely the reason for the difference from the other results.

The final comparison looks at the accuracy of the actual vortical structures being resolved within the simulation. Contours of the vorticity magnitude at the nondimensional time of $t^* = 8$, located on the plane $x = -\pi L$ and in the region bounded by the lines $y = [0, \frac{\pi L}{2}]$ and $z = [\frac{\pi L}{2}, \pi L]$, are shown in Fig. 3. Particularly, Fig. 3a shows the contours for the $\mathcal{P}4$ solution using 241^3 DoF on the tetrahedra-only grid, Fig. 3b shows the vorticity contours for the $\mathcal{P}4$ solution using 255^3 DoF on the hexahedra-only grid, Fig. 3c shows the contours for the $\mathcal{P}4$ solution using 469^3 DoF on the tetrahedra-only grid, Fig. 3d shows the vorticity contours for the $\mathcal{P}4$ solution using 510^3 DoF on the hexahedra-only grid, and Fig. 3e shows the contours from the pseudo-spectral reference solution using 512^3 DoF. The contours from both GFR solutions show nearly all of the same structures present in the spectral solution. These two comparisons show quite clearly that the unstructured capability in GFR is working correctly and accurately.

III.B. Turbulent Heat Flux Phase III

III.B.1. Experimental Geometry and Flow Conditions

The Turbulent Heat Flux Phase III (THX3) configuration from Ref. 57 was designed to create a set of detailed flow measurements of a simple single-hole film cooling flow for CFD validation and model development. The experiment, as shown in Fig. 4, consists of a convergent nozzle with a square exit blowing hot flow over an aft plate. A long single cooling flow tube is mounted below the plate and inclined 30 degrees relative to the main flow direction. The injector exit at the plate surface is therefore 2:1 elliptical and centered 1.5 pipe diameters from the nozzle exit in the middle of the plate. Particle Image Velocimetry (PIV) data is available along the symmetry plane and at several cross-planes. Raman-based temperature measurements are also available on many of those same planes, but only at a much more limited set of discrete points. In the experiment, a number of different operating conditions, or set points, were investigated. The results that follow only look at Set Point 23 from the experiment which consists of a static temperature ratio of 1.765; a nozzle pressure ratio of 1.103; and a jet exit Mach number of 0.376. Two momentum blowing ratios (BR) of 1.0 and 2.0 were explored at this set point, where the momentum blowing ratio is defined as $\text{BR} = (\rho u)_{inj}/(\rho u)_{jet}$.

III.B.2. Computational Setup

Since the unstructured grid capability was still in development, the grid used by GFR for LES of the THX3 geometry was a mesh comprising 13.1 million high-order hexahedral grid cells. The heated jet from the square nozzle was modeled using a constant-area square duct with a synthetic eddy method (SEM) inflow boundary condition along all four walls of the nozzle. The input flow profile for the SEM boundary condition was extracted from a RANS simulation at the exit of the nozzle. The length of the constant-area square duct nozzle was made sufficiently long that the boundary layer profile created by the SEM inflow approximately matched the PIV boundary layer height and mean flow conditions one injector-tube-diameter downstream of the nozzle exit. A large circular plenum pipe with correct total conditions for the injector flow was used as the inflow for the injector tube. The sharp decrease in radius from the plenum tube to the injector tube creates a forward-facing step that naturally trips the flow to create a turbulent flow in the injector tube. For

the GFR results presented in this paper, a $\mathcal{P}4$ solution containing 1.64 billion DoF was used for LES of a blowing ratio of 1.0, whereas a $\mathcal{P}3$ solution containing 839 million DoF was used for LES of a blowing ratio of 2.0. Further details about the computational setup of GFR for these simulations can be found in Ref. 18.

The LES results from GFR were compared to experimental data as well as LES results from the high-order FDL3DI code and RANS results from the FUN3D code. FDL3DI[58] is a compressible Navier-Stokes solver that is developed by the Air Force Research Laboratory at Wright-Patterson Air Force Base. It employs a sixth-order compact difference numerical scheme with spectral-like properties for spatial derivatives. An eighth-order Padé spatial filter is applied for added stability and to add dissipation in the high wave-number space, acting as an implicit sub-grid model for LES. Time integration is achieved using a second-order implicit Beam and Warming scheme which provides added stability and larger time steps. The computational mesh utilized by FDL3DI was comprised of 36 overset structured blocks with 356 million DoF; all FDL3DI results presented in this document are from simulations run on this mesh. Further details about the computational setup of FDL3DI for these simulations can be found in Ref. 59.

The FUN3D (Fully Unstructured Navier-Stokes 3D) code[60] was used to perform an assessment of various turbulence models applied to the THX3 case.[61] Here, only results from the differential SSG/LRR Reynolds Stress Model (RSM),[62,63] which solves modeled transport equations for each of the turbulent stresses and therefore had the best prospects of the RANS modeling approaches to provide an accurate prediction of this flow, are compared. A standard gradient diffusion model was used for the turbulent heat flux with the default value of 0.9 for the turbulent Prandtl number. The FUN3D simulations used a second-order Roe upwind flux difference splitting scheme, and the loosely-coupled turbulence equations were solved using a simple first-order upwind scheme. The second-order optimized time advancement option was used for integration in time until the simulation reached a steady-state solution. The FUN3D grid took advantage of half-symmetry in the spanwise direction with the final grid containing only hexahedral elements with 33.2 million grid nodes. Further details about the computational setup of FUN3D for these simulations can be found in Ref. 61.

III.B.3. Blowing Ratio of 2.0

Figure 5 compares the mean temperature contours for BR = 2.0 extracted from the various CFD solutions to the experimental data. In each of these figures, the top row are contour slices for the experimental data, the second row is from the FDL3DI time-averaged solution, the third row is from the GFR time-averaged solution, and the last row is from the FUN3D solution using RSM. The left column shows a streamwise slice taken along the plate centerline, and the seven columns on the right show cross-stream slices taken at different axial locations: from left to right, x/D of 3, 5, 7, 9, 11, 13, and 15. There is a significant difference between RANS and LES with the structure of the RANS cooling jet unlike the others. The streamwise slice shows the RANS cooling jet has completely lifted off the flat plate, whereas the LES results still appear to be attached to the plate. The Raman dataset is very sparse so it is difficult to compare contours of mean temperature with the CFD solutions. To help with this, faint white lines or boxes have been superimposed onto the CFD solutions to help illustrate where the experimental data lies within the CFD domain. Even with the coarse resolution, the LES still compares very well with the experimental data. The RANS solution is in reasonable agreement up to about $x/D = 5$ which is the location where the stronger counter-rotating vortex pair begins to lift the cooling jet off the flat plate.

To obtain a more quantitative comparison of LES and RANS to the experimental data, Fig. 6 shows flow profiles of the mean streamwise and vertical velocities as well as the mean temperature, extracted from the time-averaged LES and the FUN3D RANS solutions at four different axial stations along the plate centerline: x/D of 3, 5, 7, and 9. Looking across all the profile comparisons in Fig. 6, as well as other comparisons presented in Ref. 18, there are four general conclusions that can be made:

1. The LES solutions from GFR and FDL3DI are in close agreement for every variable examined. There are a few places where the magnitudes of the peaks and valleys differ between the two solutions; otherwise they agree both qualitatively and quantitatively. This is particularly significant because these two CFD codes used different numerical methods; grid geometries, domains, and topologies; and unsteady turbulence generators for the inflow boundary condition of the square nozzle.
2. The LES solutions compare extremely well with the experimental data for the mean variables shown in Fig. 6.

3. The LES solutions compare reasonably well with the experimental data for the turbulence variables in Ref. 18. Primarily, the LES matches the trends of the experimental data, but the magnitudes are slightly off in certain places. For example, the experimental data shows non-zero axial and vertical root-mean-square (RMS) velocity components in the potential core of the square nozzle whereas the LES computes zero velocity fluctuations. This is likely due to the unsteady inflow boundary conditions used for the LES only existing in the boundary layer. The magnitude of the RMS temperature is also very different from the Raman data, but similar findings have also been seen in previous LES of heated jets[64] when comparing to the same Raman-based measurements of temperature fluctuations.
4. RANS does a poor job of predicting the near wall temperature profiles, and has trouble matching the LES turbulent heat fluxes. The axial turbulent heat flux is most troubling where it shows a nearly zero heat flux across the entire vertical profile. The vertical heat flux is a little better but the magnitude of the near wall heat flux is significantly lower than the LES.

III.B.4. Blowing Ratio of 1.0

Figure 7 makes the same mean temperature contour comparison as from Section III.B.3 for the various CFD solutions to the experimental data. The RANS solution tends to vertically elongate the cooling jet flow which is most likely due to the stronger counter-rotating vortex pair predicted by RSM. However, the most significant result is that the GFR and FDL3DI LES solutions are nearly indistinguishable.

The same flow profiles as from Section III.B.3 were extracted for BR = 1.0, which are shown in Fig. 8. The same conclusions made for BR = 2.0 can be made for BR = 1.0, except that these conclusions are even stronger for this case. The most significant result is that the GFR and FDL3DI LES flow profiles are almost identical for the mean velocity and temperature, as well as the turbulent statistics for both; there are some small differences in the upper shear layer, but this is most likely due to slightly different boundary conditions for the nozzle exterior inflow.

More extensive results from both BR = 1.0 and BR = 2.0 simulations can be found in Ref. 18, 19, 59, 61.

III.C. Spacecraft Cabin Ventilation Fan

A new spacecraft cabin ventilation fan was designed and computationally analyzed in Ref. 65. This fan was designed to provide improved ventilation for spacecraft cabin environments with better aerodynamic and acoustic characteristics. The final fan design, shown in Fig. 9, consists of single-stage with nine rotor and eleven stator blades in a 9 in. long passage with a diameter of approximately 4 inches. Design operating conditions for the fan at 12,000 RPM specify a volumetric flow rate of 150.3 ft^3/min (CFM) and stagnation pressure rise of 3.64 in. of water at 70°F and 14.7 psia. A metal version of the design was manufactured and tested in Ref. 66 and is the source of the experimental data used in this work. This particular case was chosen for verification and validation of the new rotating turbomachinery capability in GFR because it provides a shock-free, nearly-incompressible flow on a relatively simple yet highly-curved geometry, as well as its current relevance to NASA with the physical model being tested locally at NASA Glenn Research Center.

GFR currently does not have a sliding interface capability which is required to run the full rotor-stator geometry; therefore, this case was reduced to a rotor only configuration. To further reduce the computational cost of running an LES, a rotationally periodic domain of 40° was created around a single rotor blade. The meridional view of the fan system shown in Fig. 9a includes three colored lines to indicate where the GFR computational domain, shown in Fig. 10, is in relation to the physical geometry. The blue line in Fig. 9a is the axial location of the inflow plane for GFR. The blue surface in Fig. 10 is where the hub geometry was modified slightly to facilitate a more stable flow near the inflow since rotated periodic boundaries precludes the inclusion of the nose fairing geometry in the GFR simulations. The thin black surface behind the blade in Fig. 10 is the physical air gap between the rotating and stationary parts of the hub which has been filled in with a wall boundary for these simulations; this roughly corresponds to the dashed black line in Fig. 9a. Finally, the green section at the right of Fig. 10 is the sponge region added on to the outflow boundary to help damp out non-physical pressure waves from reflecting off the outflow boundary. In Fig. 9a, the green and red lines represent the axial locations where the sponge region respectively begins and ends; the GFR grid did not include the part of the stator blade that lies inside the sponge region.

Fidelity Pointwise was again utilized to generate the unstructured mixed-element mesh for this case. The advancing front unstructured algorithm was used for the generation of the surface meshes containing

a mixture of triangle and quadrilateral elements. For each surface element on the rotor and hub wall boundaries, the approximate edge length in wall units (denoted by the superscript +) is shown in Fig. 11. For quadrilateral surface elements, the edge length, l, is computed as $l = \sqrt{A}$, where A is the area of the element. The edge length for triangle surface elements is based on an equilateral triangle assumption where $l = \sqrt{4A/\sqrt{3}}$. The top view on the left of Fig. 11 shows that the average element spacing along the hub varies between 70 and 100 wall units. The views of the pressure and suction sides of the rotor blade on the right side of Fig. 11 show the edge lengths along the mid-span to vary between 45 and 75 wall units, and the hub fillet and rotor tip edge lengths to vary between 5 and 30 wall units. The volume mesh was generated from the surface mesh using the T-Rex grid generation algorithm with the wall spacing set to 0.0002 inches. This value was found to be approximately $y^+ = 1$ based on the skin friction extracted from prior RANS simulations[67] on the mid-span suction surface of the rotor blade. The volume elements have a characteristic length of 0.014 in. or roughly 70 wall units. The final grid contains a total of 2,323,333 elements comprised of 820,641 tetrahedra, 56,611 pyramids, 1,109,372 prisms, and 336,709 hexahedra.

All solid wall boundaries were set to an adiabatic no-slip wall boundary condition. The outer case wall was specified as non-rotating in the inertial reference frame, and the inner hub and blade surfaces were set to the fan rotation speed of 12,000 RPM by specifying them as non-rotating in the rotating reference frame. In all of the GFR results, the entire hub surface is rotating with the rotor blade, including the stationary part of the hub from the physical model that is included in the GFR computational domain, i.e., the hub surfaces to the right of the thin black surface in Fig. 10. The inflow conditions were set to match those used in Ref. 67 with a Mach number of 0.033, static temperature of 70°F, and stagnation pressure of 14.8 psia. The static pressure at the outflow boundary was set to achieve a specified static pressure ratio (SPR) relative to the inflow.

A series of $\mathcal{P}1$ simulations with varying SPR were run to create an initial fan performance map to quickly identify peak operating and stall points. At $\mathcal{P}1$, the simulations contained 12.9 million DoF. Each individual case was run until the volumetric flow rate stabilized or, in the case of stall, began to diverge. A plot of volumetric flow rate versus the number of full revolutions completed by the simulation for each of the operating points is shown in Fig. 12a, and Fig. 12b shows a plot of the rise in stagnation pressure across the rotor during the same simulation time. It is clear that the two cases with SPR's of 1.00775 and 1.0078 started to diverge and show signs of stalling; this was additionally confirmed with visualizations of the solution showing the majority of the flow in the upper third of the blade span reversing direction axially and starting to flow upstream.

In order to create the fan performance map, averages for each of the lines in Fig. 12 were made to get the data for the individual operating points. Care was taken to only average what appeared to be the converged part of each time history plot. Additionally, averages were taken of the time history for the total or stagnation pressure ratio, TPR, and stagnation temperature ratio, TTR, to compute the adiabatic efficiency, η, for each operating point using

$$\eta = \frac{\mathrm{TPR}^{\frac{\gamma-1}{\gamma}} - 1}{\mathrm{TTR} - 1} \tag{18}$$

Figure 13 shows the fan performance map at 12,000 RPM obtained by all the $\mathcal{P}1$ simulations that did not stall. Figure 13a shows the stagnation pressure rise versus volumetric flow rate of the $\mathcal{P}1$ simulations compared to the experiment. The GFR map is not intended to match the experimental data because these simulations are rotor-only, and the fan performance map from the experiment was obtained from the full rotor-stator geometry; it merely serves as a gauge to show that the GFR results are within reason. Figure 13b shows the computed adiabatic efficiency for each $\mathcal{P}1$ simulation versus volumetric flow rate. Two data points that can be compared to the design operating condition and experimental data are the volumetric flow rates at the peak efficiency and peak stagnation pressure rise. The peak efficiency found by GFR occurs using a SPR of 1.0055 resulting in a volumetric flow rate of 144 CFM, which is very near the design flow rate of 150 CFM. The volumetric flow rate at peak stagnation pressure rise was found to be 110 CFM using a SPR of 1.0077, with any further increase to the SPR causing the rotor to stall; the experiment also found stall at 110 CFM.

The peak efficiency and peak pressure rise operating points were singled out for further analysis at higher order. For both cases, the $\mathcal{P}1$ result was used as the initialization for the higher-order simulations. The peak efficiency operating point was run at $\mathcal{P}3$ for 0.48 revolutions, and then a time average of the flow including

mean and turbulent quantities was collected by running the simulation for a further 1.6 revolutions. Detailed analysis of this time-averaged flow, particularly how it compares to RANS and experimental results, will be the subject of future work. This simulation did reach a converged volumetric flow rate so the stagnation pressure rise and adiabatic efficiency were computed and included on the plots in Fig. 13 to see how the $\mathcal{P}3$ values compare to the original $\mathcal{P}1$ results for the same operating point. All three quantities are higher at $\mathcal{P}3$ than what was found at $\mathcal{P}1$, with the increases being 12% for volumetric flow rate, 16% for stagnation pressure rise, and 8% for adiabatic efficiency. This is the expected result as the higher numerical dissipation present in the lower-order $\mathcal{P}1$ simulation can be thought of as an additional loss to the flow.

The SPR achieving the peak pressure rise was used to explore the difference in resolved turbulent flow structures between solutions with different orders of accuracy. The final $\mathcal{P}1$ solution at SPR = 1.0077 used in evaluating the fan performance map from Figs. 12 and 13 was used as the initialization for four additional simulations with solution orders ranging from $\mathcal{P}1$ to $\mathcal{P}4$. These four simulations were run until a common number of revolutions were completed so that a true comparison of the instantaneous flow could be made between the different orders of accuracy. The common number of completed revolutions, 0.2522, was chosen simply because that was the furthest the $\mathcal{P}4$ simulation was able to run due to the availability of computational resources; it was deemed sufficiently long enough that the majority of transients from the initial $\mathcal{P}1$ solution have been removed from the flow. This operating point was chosen for closer study because it is close to the stall point—the difference between this point and the stall SPR is only a 0.00074 psia difference in the static back pressure—and the interest was in whether the change in solution accuracy would push the simulation towards a more stable condition or towards stall. Figure 14 shows instantaneous contours of radial velocity from each of these four simulations along isosurfaces of 99% passage height, which places the surface within the tip gap. Finally, Fig. 15 shows contours of axial velocity from the $\mathcal{P}4$ case along isosurfaces of 1%, 50%, and 100% passage height for the peak pressure rise operating point. Future work includes running these higher-order simulations further in time to find where they ultimately fall on the fan performance map as well as to create time-averaged solutions for more detailed analysis of the flow.

IV. Summary and Conclusions

The Glenn Flux Reconstruction (GFR) code is a computational fluid dynamics (CFD) code under development at NASA Glenn Research Center. GFR is based on the high-order flux reconstruction (FR) method and provides a large-eddy simulation (LES) capability that is both accurate and efficient for complex aeropropulsion flows. Three significant new capabilities have been added to the code that improve its performance and functionality.

A total of 22 explicit Runge-Kutta (ERK) methods were added to GFR to explore a variety of different time-stepping schemes of varying order, accuracy, and complexity with the goal of identifying any methods that can improve the total time-to-solution for costly LES. Four methods show a 20% or greater improvement in time-to-solution compared to the current default 3^{rd}-order/3-stage Strong Stability Preserving (SSP) Runge-Kutta (SSPRK) scheme, SSP3. The 5-stage/4^{th}-order SSPRK method, which has existed in GFR from the start, was found to be 22% faster than the SSP3 scheme. The new 11-stage/3^{rd}-order and 15-stage/4^{th}-order vortex-optimized ERK schemes both offer a 33% improvement in time-to-solution compared to the default SSP3 scheme; the 11-stage/3^{rd}-order scheme has become the new default time-stepping method in GFR. Finally, the 9-stage/4^{th}-order embedded-pair ERK method with embedded 3^{rd}-order scheme was found to be 22% faster than the SSP3 scheme.

An unstructured, mixed-element mesh capability was added to GFR. Advanced quadrature rules were added for cell types that are not able to utilize a tensor-product formulation without adding a directional bias, i.e., triangles and tetrahedra. Quadrature rules for pyramids and prisms were added by utilizing tensor products of two-dimensional and one-dimensional quadrature rules. The new mixed-element capability was validated by running the Taylor-Green vortex problem on a series of grids containing different grid topologies. The kinetic energy dissipation rate (KEDR) computed from the various grids containing only a single element type and the KEDR computed from the mixed-element grid all showed very similar magnitudes and trends for both resolutions that were examined. Furthermore, contours of the instantaneous vorticity magnitude at $t^* = 8$ were extracted from $\mathcal{P}4$ tetrahedra-only simulations containing 241^3 degrees of freedom (DoF) and 469^3 DoF which were compared against previous $\mathcal{P}4$ hexahedra-only simulations containing 255^3 DoF and 510^3 DoF, as well as the reference solution found using a pseudo-spectral code with 512^3 DoF.

A rotating turbomachinery capability was added to GFR by modifying the governing equations to a

rotating, or non-inertial, reference frame formulation written in terms of the absolute velocity. This formulation requires only a few isolated code changes while also being more amenable to a future sliding interface capability. Verification and validation of the new rotating turbomachinery capability was achieved through a series of simulations for a ventilation fan designed for better aerodynamic and acoustic performance in spacecraft cabin environments; the mixed-element grid used for these simulations also served as further verification of the unstructured capability. A fan performance map at the design speed of 12,000 RPM was generated from 16 different $\mathcal{P}1$ simulations which varied the static pressure ratio specified between the inflow and outflow boundary conditions from 1.0025 to 1.0078. The GFR fan map found a peak adiabatic efficiency at a volumetric flow rate of about 144 ft^3/min (CFM) which is very near the designed operating point of 150 CFM. Additionally, a SPR of 1.0077 resulted in the peak stagnation pressure rise of 110 CFM, in agreement with the experiment, with further increases causing the rotor to stall. Finally, the operating points of peak adiabatic efficiency and peak stagnation pressure rise were chosen for further simulations at higher orders of accuracy to demonstrate how increasing $\mathcal{P}$ improves the quality of the solution.

Future code development work includes adding a sliding interface capability to GFR, which will significantly expand the types of turbomachinery cases to which GFR may be applied. The addition of sliding interfaces will almost certainly require the ability to handle either non-matching cell interfaces or overset grids, either of which will unlock new gridding strategies to more precisely tailor grid resolution for complex flows with highly varying length scales. Other areas of interest for future code development include improving code performance through the use of General-Purpose Graphical Processing Units (GPGPUs), improved shock-capturing methods, and wall-modeled LES to reduce the near-wall grid resolution required for flows at higher Reynolds numbers.

V. Acknowledgments

This research was sponsored by NASA's Transformational Tools and Technologies (TTT) Project of the Transformative Aeronautics Concepts Program under the Aeronautics Research Mission Directorate. Resources supporting this work were provided by the NASA High-End Computing (HEC) Program through the NASA Advanced Supercomputing (NAS) Division at Ames Research Center.

References

[1]Slotnick, J. P., Khodadoust, A., Alonso, J., Darmofal, D., Gropp, W., Lurie, E., and Mavriplis, D. J., "CFD Vision 2030 Study: A Path to Revolutionary Computational Aerosciences," NASA CR-2014-218178, Mar 2014.

[2]Anand, M., Medic, G., Paliath, U., Suder, K. L., Malik, M. R., and Laskowski, G. M., "Vision 2030 Aircraft Propulsion Grand Challenge Problem: Full-engine CFD Simulations with High Geometric Fidelity and Physics Accuracy," AIAA Paper 2021-0956, 2021.

[3]Tucker, P. G. and Wang, Z.-N., "Eddy Resolving Strategies in Turbomachinery and Peripheral Components," *Journal of Turbomachinery*, Vol. 143, No. 1, 2021, pp. 010801.

[4]DeBonis, J., "Progress Towards Large-Eddy Simulations for Prediction of Realistic Nozzle Systems," *AIAA Journal of Propulsion and Power*, Vol. 23, No. 5, 2007, pp. 971–980.

[5]Nastase, C. R. and Mavriplis, D. J., "High-Order Discontinuous Galerkin Methods Using an hp-Multigrid Approach," *Journal of Computational Physics*, Vol. 213, No. 1, 2006, pp. 330–357.

[6]Cockburn, B., Karniadakis, G. E., and Shu, C.-W., *Discontinuous Galerkin Methods: Theory, Computation, and Application*, Lecture Notes in Computational Science and Engineering, Springer, 1st ed., 2000.

[7]Murman, S. M., Diosady, L., Garai, A., and Ceze, M., "A Space-Time Discontinuous-Galerkin Approach for Separated Flows," AIAA Paper 2016-1059, 2016.

[8]Huynh, H., "A Flux Reconstruction Approach to High-Order Schemes Including Discontinuous Galerkin Methods," AIAA Paper 2007-4079, Jun 2007.

[9]Huynh, H., "A Reconstruction Approach to High-Order Schemes Including Discontinuous Galerkin for Diffusion," AIAA Paper 2009-403, Jan 2009.

[10]Huynh, H., "High-Order Methods Including Discontinuous Galerkin by Reconstructions on Triangular Meshes," AIAA Paper 2011-44, Jan 2011.

[11]Vermeire, B. C., Cagnone, J.-S., and Nadarajah, S., "ILES Using the Correction Procedure via Reconstruction Scheme," AIAA Paper 2013-1001, Jan 2013.

[12]Vermeire, B. C., Nadarajah, S., and Tucker, P. G., "Canonical Test Cases for High-Order Unstructured Implicit Large Eddy Simulation," AIAA Paper 2014-0935, Jan 2014.

[13]Skarolek, V. and Miyaji, K., "Transitional Flow over a SD7003 Wing Using Flux Reconstruction Scheme," AIAA Paper 2014-0250, Jan 2014.

[14]Haga, T., Tsutsumi, S., Kawai, S., and Takaki, R., "Large-Eddy Simulation of a Supersonic Jet Using High-Order Flux Reconstruction Scheme," AIAA Paper 2015-0831, Jan 2015.

[15]Wang, Z., Li, Y., Jia, F., Laskowski, G., Kopriva, J., Paliath, U., and Bhaskaran, R., "Towards Industrial Large Eddy Simulation Using the FR/CPR Method," *Computers & Fluids*, Vol. 156, 2017, pp. 579–589.

[16]Shi, J., Yan, H., and Wang, Z., "Flux Reconstruction Implementation of an Algebraic Wall Model for Large-Eddy Simulation," *AIAA Journal*, Vol. 58, No. 7, 2020, pp. 3051–3062.

[17]Zhu, H., Fu, S., Shi, L., and Wang, Z., "Implicit Large-Eddy Simulation for the High-Order Flux Reconstruction Method," *AIAA Journal*, Vol. 54, No. 9, 2016, pp. 2721–2733.

[18]Spiegel, S. C., Borghi Jr., M. R., and Yoder, D. A., "Large Eddy Simulations of a Single-Injector Cooling Flow Using the High-Order Flux Reconstruction Method," AIAA Paper 2022-1813, Jan 2022.

[19]Borghi Jr., M. R., Spiegel, S. C., Yoder, D. A., Georgiadis, N., and Wernet, M., "Turbulent Simulations of Cooling Jets in Crossflow," AIAA Paper 2022-1815, Jan 2022.

[20]Spiegel, S., DeBonis, J. R., and Huynh, H. T., "Overview of the NASA Glenn Flux Reconstruction Based High-Order Unstructured Grid Code," AIAA Paper 2016-1061, Jan 2016.

[21]Spiegel, S., Huynh, H. T., and DeBonis, J. R., "A Survey of the Isentropic Euler Vortex Problem Using High-Order Methods," AIAA Paper 2015-2444, Jun 2015.

[22]Gottlieb, S. and Shu, C.-W., "Total Variation Diminishing Runge-Kutta Schemes," *Mathematics of Computation*, Vol. 67, No. 221, 1998, pp. 73–85.

[23]Spiteri, R. J. and Ruuth, S. J., "A New Class of Optimal High-Order Strong-Stability-Preserving Time Discretization Methods," *SIAM Journal on Numerical Analysis*, Vol. 40, No. 2, 2002, pp. 469–491.

[24]Carpenter, M. H. and Kennedy, C. A., "Fourth-Order 2N-Storage Runge-Kutta Schemes," NASA TM-1994-109112, 1994.

[25]Al Jahdali, R., Dalcin, L., Boukharfane, R., Nolasco, I. R., Keyes, D. E., and Parsani, M., "Optimized Explicit Runge–Kutta Schemes for High-Order Collocated Discontinuous Galerkin Methods for Compressible Fluid Dynamics," *Computers & Mathematics with Applications*, Vol. 118, 2022, pp. 1–17.

[26]Ketcheson, D. I., "Runge–Kutta Methods with Minimum Storage Implementations," *Journal of Computational Physics*, Vol. 229, No. 5, 2010, pp. 1763–1773.

[27]Berzins, M., "Temporal Error Control for Convection-Dominated Equations in Two Space Dimensions," *SIAM Journal on Scientific Computing*, Vol. 16, No. 3, 1995, pp. 558–580.

[28]Ware, J. and Berzins, M., "Adaptive Finite Volume Methods for Time-Dependent PDEs," *Modeling, Mesh Generation, and Adaptive Numerical Methods for Partial Differential Equations*, Springer, 1995, pp. 417–430.

[29]Ranocha, H., Dalcin, L., Parsani, M., and Ketcheson, D. I., "Optimized Runge-Kutta Methods with Automatic Step Size Control for Compressible Computational Fluid Dynamics," *Communications on Applied Mathematics and Computation*, Vol. 4, No. 4, 2022, pp. 1191–1228.

[30]Dormand, J. R. and Prince, P. J., "A Family of Embedded Runge-Kutta Formulae," *Journal of Computational and Applied Mathematics*, Vol. 6, No. 1, 1980, pp. 19–26.

[31]Prince, P. J. and Dormand, J. R., "High Order Embedded Runge-Kutta Formulae," *Journal of Computational and Applied Mathematics*, Vol. 7, No. 1, 1981, pp. 67–75.

[32]Hairer, E., Norsett, S., and Wanner, G., *Solving Ordinary Differential Equations I. Nonstiff Problems*, Springer Series in Computational Mathematics, Springer-Verlag, 2nd ed., 1993.

[33]Brachet, M. E., Meiron, D. I., Orszag, S. A., Nickel, B., Morf, R. H., and Frisch, U., "Small-Scale Structure of the Taylor–Green Vortex," *Journal of Fluid Mechanics*, Vol. 130, 1983, pp. 411–452.

[34]van Rees, W. M., Leonard, A., Pullin, D. I., and Koumoutsakos, P., "A Comparison of Vortex and Pseudo-Spectral Methods for the Simulation of Periodic Vortical Flows at High Reynolds Numbers," *Journal of Computational Physics*, Vol. 230, 2011, pp. 2794–2805.

[35]Wang, Z., Fidkowski, K., Abgrall, R., Bassi, F., Caraeni, D., Cary, A., Deconinck, H., Hartmann, R., Hillewaert, K., Huynh, H., Kroll, N., May, G., Persson, P.-O., van Leer, B., and Visbal, M., "High-order CFD Methods: Current Status and Perspective," *International Journal for Numerical Methods in Fluids*, Vol. 72, No. 8, 2013, pp. 811–845.

[36]Spiegel, S., Huynh, H. T., and DeBonis, J. R., "De-Aliasing through Over-Integration Applied to the Flux Reconstruction and Discontinuous Galerkin Methods," AIAA Paper 2015-2744, Jun 2015.

[37]Williams, D. M. and Jameson, A., "Nodal Points and the Nonlinear Stability of High-Order Methods for Unsteady Flow Problems on Tetrahedral Meshes," AIAA Paper 2013-2830, Jun 2013.

[38]Yu, M., Wang, Z., and Liu, Y., "On the Accuracy and Efficiency of Discontinuous Galerkin, Spectral Difference and Correction Procedure via Reconstruction Methods," *Journal of Computational Physics*, Vol. 259, 2014, pp. 70–95.

[39]Witherden, F. D. and Vincent, P. E., "An Analysis of Solution Point Coordinates for Flux Reconstruction Schemes on Triangular Elements," *Journal of Scientific Computing*, Vol. 61, No. 2, 2014, pp. 398–423.

[40]Witherden, F. D. and Vincent, P. E., "On the Identification of Symmetric Quadrature Rules for Finite Element Methods," *Computers & Mathematics with Applications*, Vol. 69, No. 10, 2015, pp. 1232–1241.

[41]Witherden, F. D., Park, J. S., and Vincent, P. E., "An Analysis of Solution Point Coordinates for Flux Reconstruction Schemes on Tetrahedral Elements," *Journal of Scientific Computing*, Vol. 69, 2016, pp. 905–920.

[42]Chen, Q. and Babuška, I., "Approximate Optimal Points for Polynomial Interpolation of Real Functions in an Interval and in a Triangle," *Computer Methods in Applied Mechanics and Engineering*, Vol. 128, No. 3-4, 1995, pp. 405–417.

[43]Hesthaven, J. S., "From Electrostatics to Almost Optimal Nodal Sets for Polynomial Interpolation in a Simplex," *SIAM Journal on Numerical Analysis*, Vol. 35, No. 2, 1998, pp. 655–676.

[44]Taylor, M. A., Wingate, B. A., and Vincent, R. E., "An Algorithm for Computing Fekete Points in the Triangle," *SIAM Journal on Numerical Analysis*, Vol. 38, No. 5, 2000, pp. 1707–1720.

[45]Taylor, M. A., Wingate, B. A., and Bos, L. P., "Several New Quadrature Formulas for Polynomial Integration in the Triangle," *arXiv preprint math/0501496*, 2005.

[46]Wandzurat, S. and Xiao, H., "Symmetric Quadrature Rules on a Triangle," *Computers & Mathematics with Applications*, Vol. 45, No. 12, 2003, pp. 1829–1840.

[47]Kubatko, E. J., Yeager, B. A., and Maggi, A. L., "New Computationally Efficient Quadrature Formulas for Pyramidal Elements," *Finite Elements in Analysis and Design*, Vol. 65, 2013, pp. 63–75.

[48]Kubatko, E. J., Yeager, B. A., and Maggi, A. L., "New Computationally Efficient Quadrature Formulas for Triangular Prism Elements," *Computers & Fluids*, Vol. 73, 2013, pp. 187–201.

[49]Williams, D. M., *Energy Stable High-Order Methods for Simulating Unsteady, Viscous, Compressible Flows on Unstructured Grids*, Stanford University, 2013.

[50]Shunn, L. and Ham, F., "Symmetric Quadrature Rules for Tetrahedra Based on a Cubic Close-Packed Lattice Arrangement," *Journal of Computational and Applied Mathematics*, Vol. 236, No. 17, 2012, pp. 4348–4364.

[51]Abe, Y., Haga, T., Nonomura, T., and Fujii, K., "Fully-Conservative High-Order FR Scheme on Moving and Deforming Grids," AIAA Paper 2015-2745, 2015.

[52]Chima, R. V. and Yokota, J. W., "Numerical Analysis of Three-Dimensional Viscous Internal Flows," *AIAA journal*, Vol. 28, No. 5, 1990, pp. 798–806.

[53]Chen, J., Ghosh, A., Sreenivas, K., and Whitfield, D., "Comparison of Computations Using Navier-Stokes Equations in Rotating and Fixed Coordinates for Flow Through Turbomachinery," AIAA Paper 1997-878, 1997.

[54]Biedron, R. and Thomas, J., "Recent Enhancements to the FUN3D Flow Solver for Moving-Mesh Applications," AIAA Paper 2009-1360, 2009.

[55]Silva, P. A., Tsoutsanis, P., and Antoniadis, A. F., "Simple Multiple Reference Frame for High-Order Solution of Hovering Rotors with and without Ground Effect," *Aerospace Science and Technology*, Vol. 111, 2021, pp. 106518.

[56]DeBonis, J. R., "Solutions of the Taylor-Green Vortex Problem Using High-Resolution Explicit Finite Difference Methods," AIAA Paper 2013-0382, Jan 2013.

[57]Wernet, M. P., Georgiadis, N. J., and Locke, R. J., "PIV and Rotational Raman-Based Temperature Measurements for CFD Validation in a Single Injector Cooling Flow," NASA TM-2018-219739, Jan 2018.

[58]Gaitonde, D. V. and Visbal, M. R., "High-order Schemes for Navier-Stokes Equations: Algorithm and Implementation into FDL3DI," Tech. rep., Air Force Research Lab Wright-Patterson AFB OH Air Vehicles Directorate, 1998.

[59]Borghi Jr., M. R., "Implicit Large-Eddy Simulation of Single-Injector Cooling Flow," AIAA Paper 2022-1814, Jan 2022.

[60]Biedron, R. T., Carlson, J. R., Derlaga, J. M., Gnoffo, P. A., Hammond, D. P., Jones, W. T., Kleb, B., Lee-Rausch, E. M., Nielsen, E. J., Park, M. A., Rumsey, C. L., Thomas, J. L., Thompson, K. B., and Wood, W. A., "FUN3D Manual: 13.6," NASA TM-2019-220416, Oct 2019.

[61]Yoder, D. A., "Assessment of Turbulence Models for a Single-Injector Cooling Flow," AIAA Paper 2022-1812, Jan 2022.

[62]Eisfeld, B., Rumsey, C., and Togit, V., "Verification and Validation of a Second-Moment-Closure Model," *AIAA Journal*, Vol. 54, No. 2, 2016, pp. 1524–1541.

[63]Eisfeld, B., Rumsey, C., and Togit, V., "Verification and Validation of a Second-Moment-Closure Model," *AIAA Journal*, Vol. 54, No. 9, 2016, pp. 2926.

[64]DeBonis, J. R., "Prediction of Turbulent Temperature Fluctuations in Hot Jets," AIAA Paper 2017-3610, Jun 2017.

[65]Tweedt, D. L., "Aerodynamic Design and Computational Analysis of a Spacecraft Cabin Ventilation Fan," NASA CR-2010-216329, Dec 2010.

[66]Stephens, D., Goodman, J., Buehrle, R., Koch, L. D., and Sutliff, D., "Aerodynamic and Acoustic Performance Testing of Metal Spacecraft Cabin Ventilation Fan," NASA TM-20230001811, Aug 2023.

[67]Butler, B. A., Valentin-Cruz, C. A., Borghi Jr., M. R., and Turner, M. G., "Full Stall Simulations of a Redesigned Ventilation Fan for the ISS," AIAA Paper 2023-1755, Jan 2023.

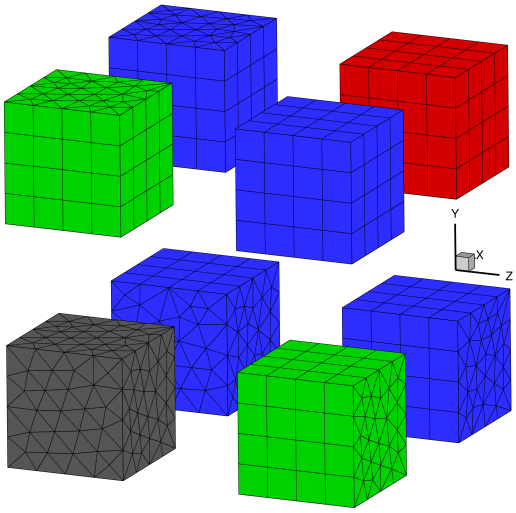

Figure 1: Exploded view of the eight sub-blocks or octants that combine to create one of the mixed element grids for the Taylor-Green vortex problem. The red block contains only hexahedra cells, the green blocks contain only prism cells, the gray block contains only tetrahedra cells, and the blue blocks contain a mixture of tetrahedra and pyramid cells.

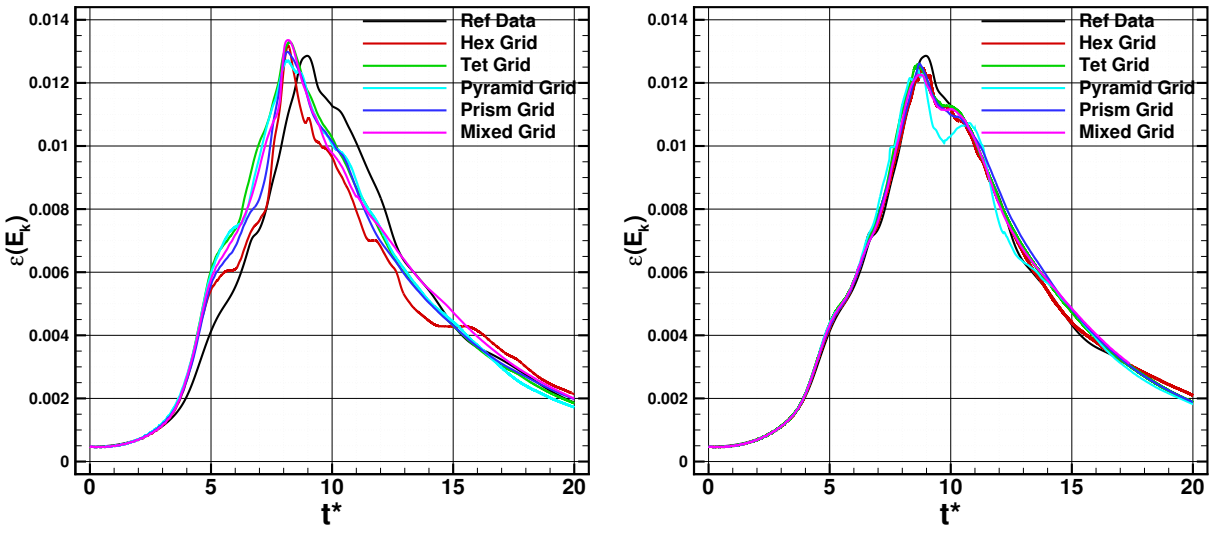

(a) $\mathcal{P}3$ with approximately 64^3 DoF.

(b) $\mathcal{P}4$ with approximately 128^3 DoF.

Figure 2: Comparison of the kinetic energy dissipation rate (KEDR) results for $\mathcal{P}3$ and $\mathcal{P}4$ simulations on grids with different topologies.

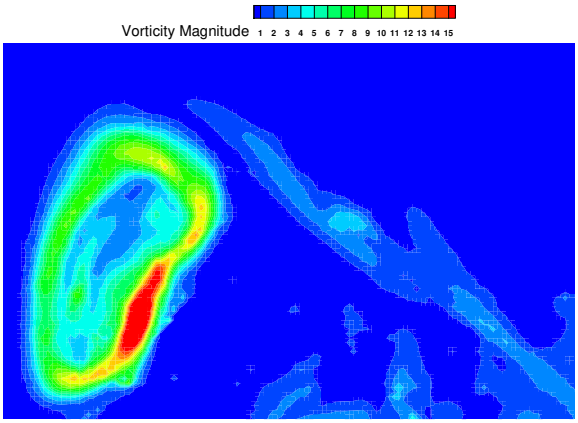

(a) $\mathcal{P}4$ using 241^3 DoF on a tetrahedra-only grid.

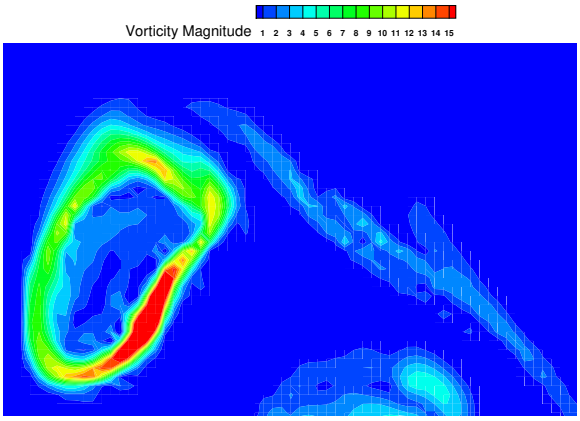

(b) $\mathcal{P}4$ using 255^3 DoF on a hexahedra-only grid.

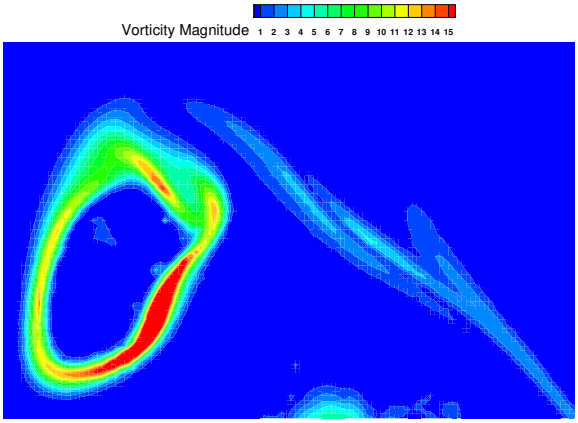

(c) $\mathcal{P}4$ using 469^3 DoF on a tetrahedra-only grid.

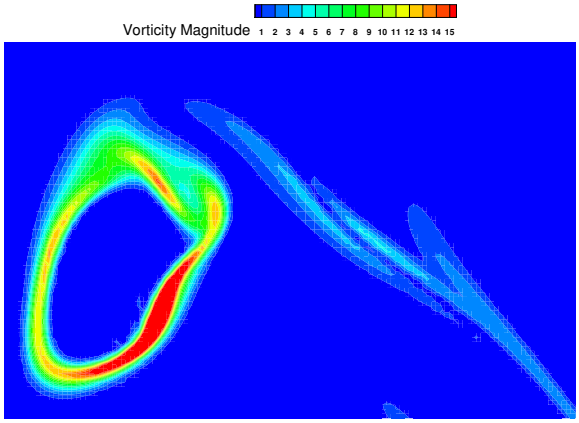

(d) $\mathcal{P}4$ using 510^3 DoF on a hexahedra-only grid.

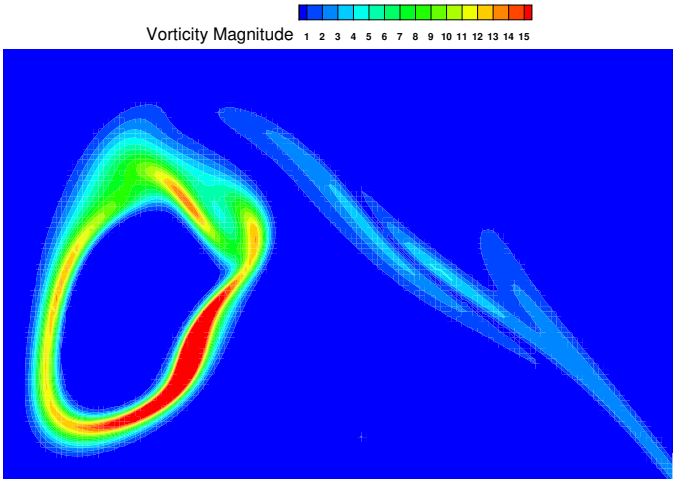

(e) Reference solution found using a pseudo-spectral code with 512^3 DoF.

Figure 3: Contours of vorticity norm at $t^* = 8$ on the plane $x = -\pi L$, in the region bounded by the lines $y = [0, \frac{\pi L}{2}]$ and $z = [\frac{\pi L}{2}, \pi L]$.

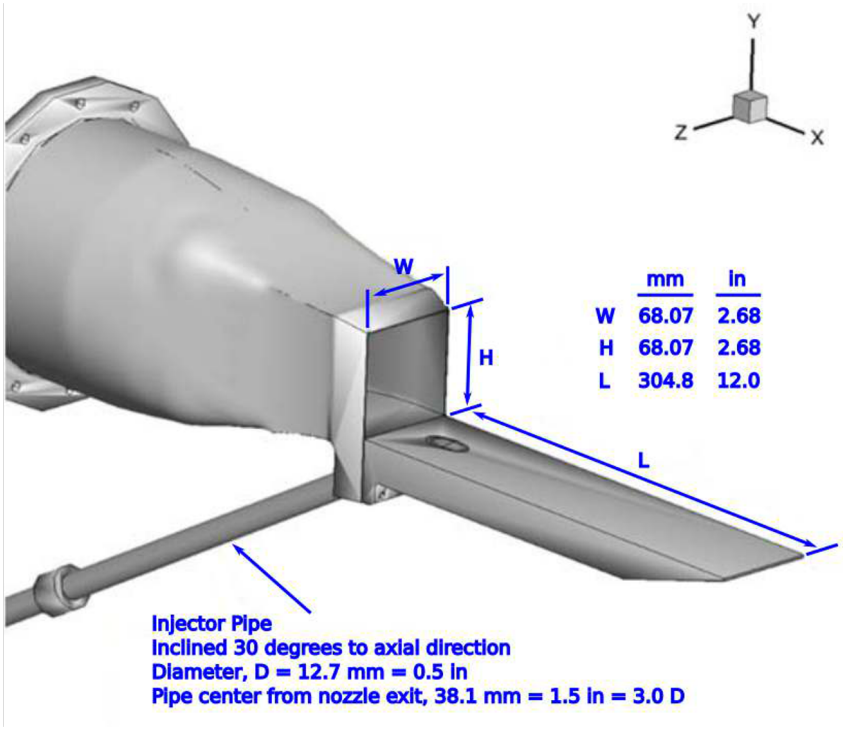

Figure 4: Experimental geometric configuration.

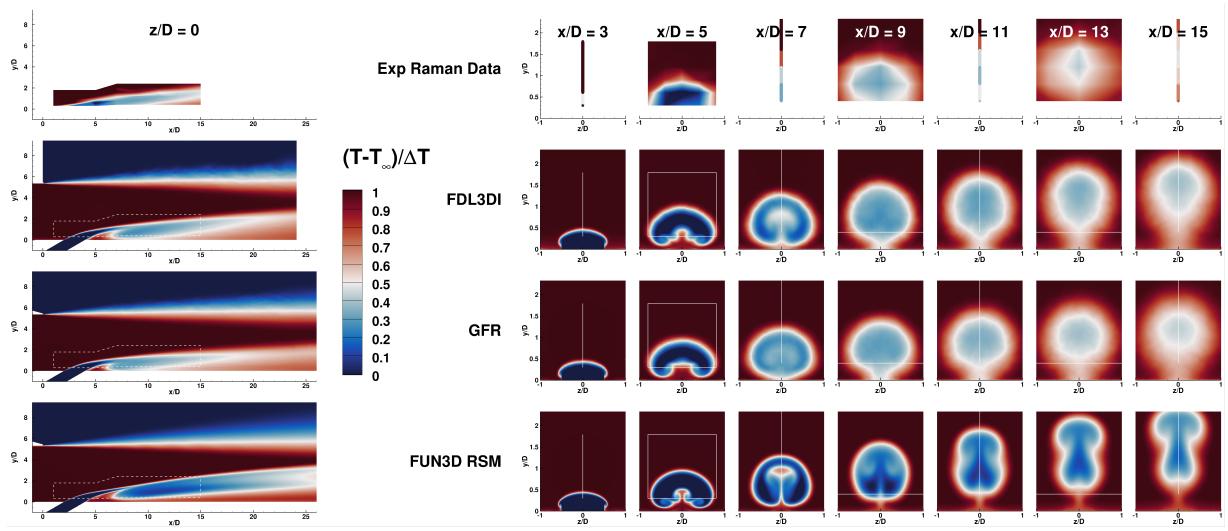

Figure 5: Comparison of mean temperature contours between experiment, LES from FDL3DI, LES from GFR, and RANS from FUN3D for BR = 2.0. The left column compares a streamwise slice taken along the plate centerline. The other columns compare cross-stream slices taken from multiple axial locations along the plate. Thin white lines are superimposed onto the CFD contours to help illustrate where the experiment data lies within the CFD data.

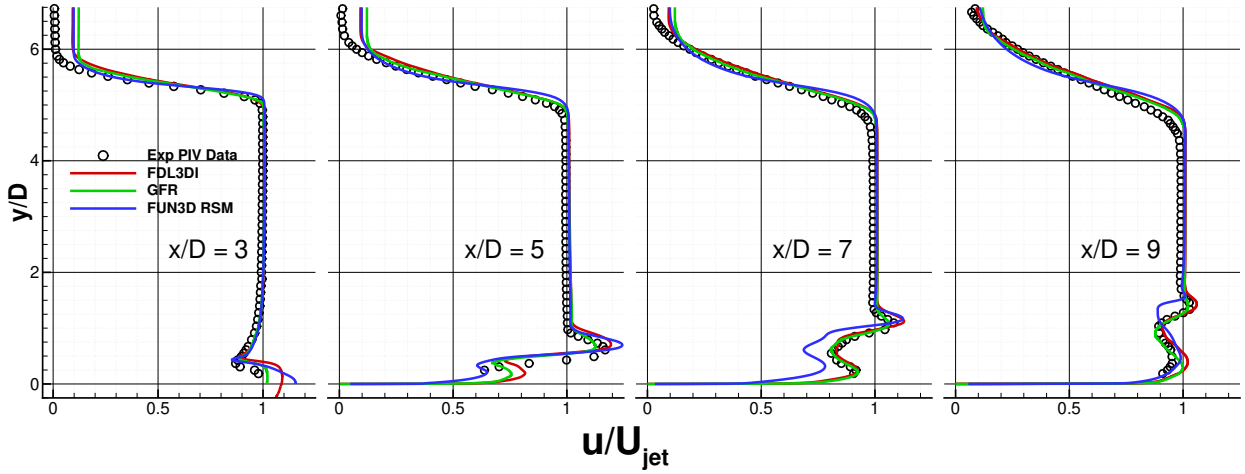

(a) Mean streamwise velocity profiles for BR = 2.0.

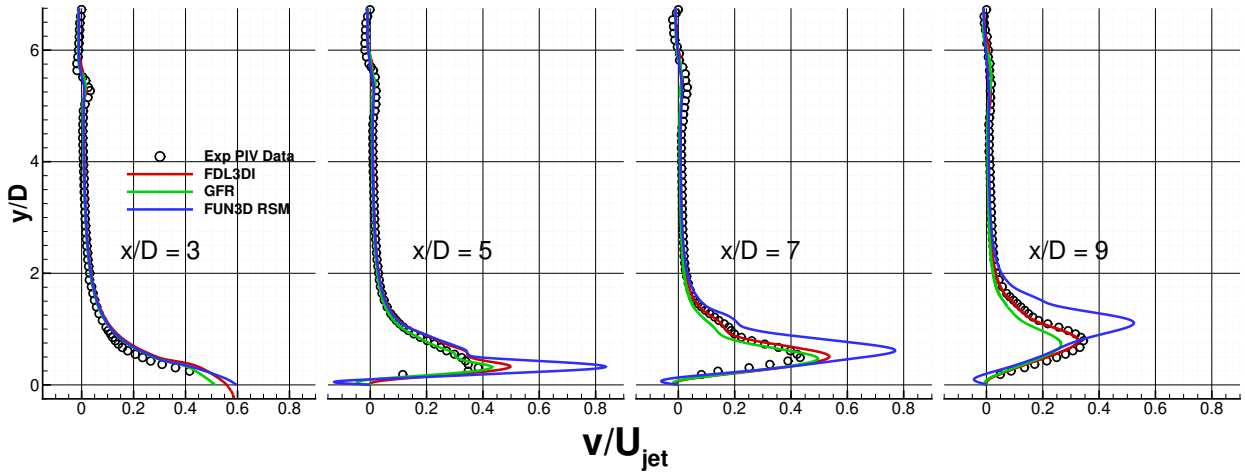

(b) Mean vertical velocity profiles for BR = 2.0.

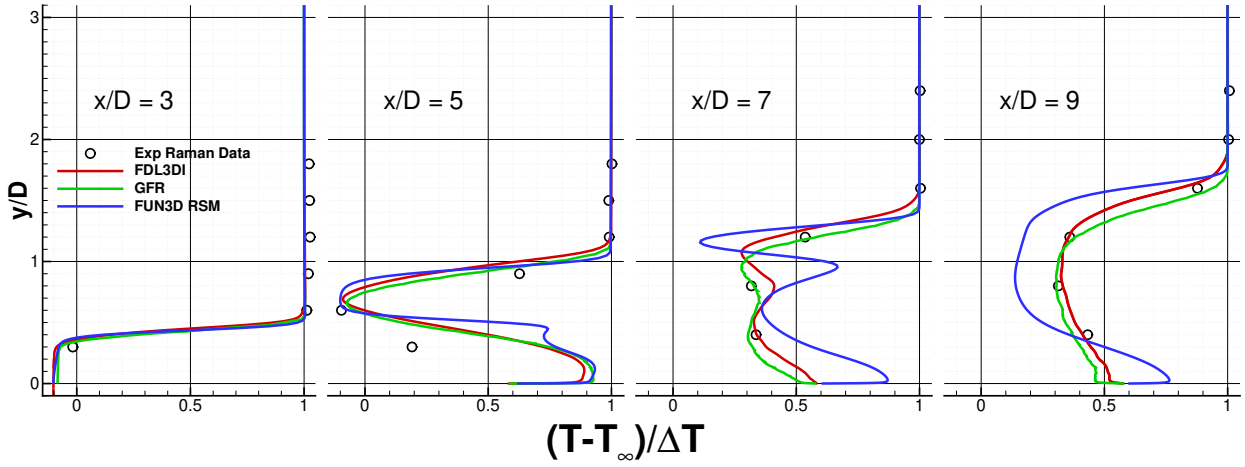

(c) Mean temperature profiles for BR = 2.0.

Figure 6: Comparison between experiment, LES from FDL3DI, LES from GFR, and RANS from FUN3D of 1D profiles of mean variables taken at various axial locations along the plate centerline for BR = 2.0.

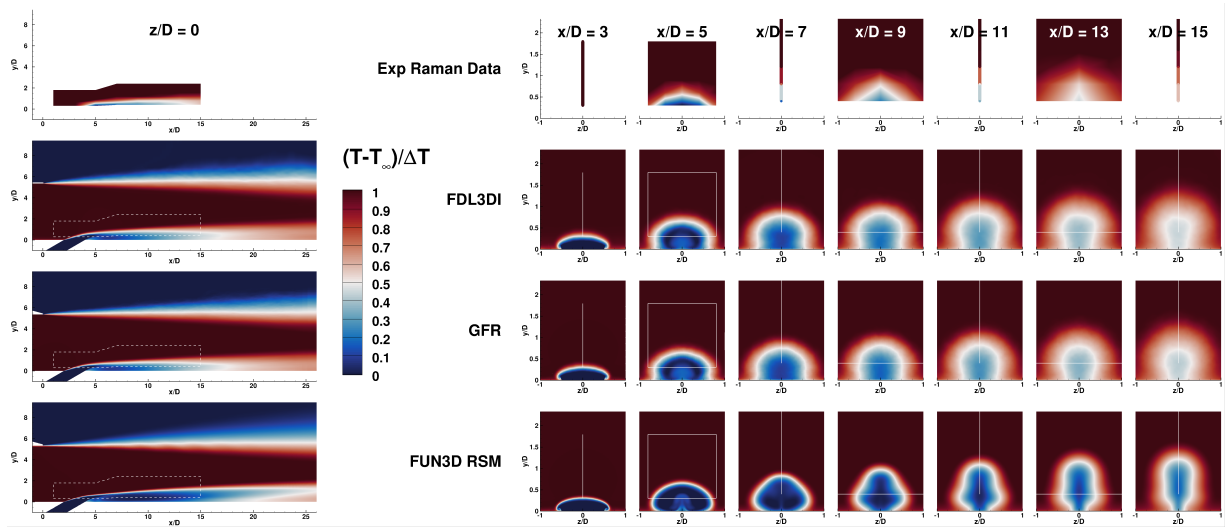

Figure 7: Comparison of mean temperature contours between experiment, LES from FDL3DI, LES from GFR, and RANS from FUN3D for BR = 1.0. The left column compares a streamwise slice taken along the plate centerline. The other columns compare cross-stream slices taken from multiple axial locations along the plate. Thin white lines are superimposed onto the CFD contours to help illustrate where the experiment data lies within the CFD data.

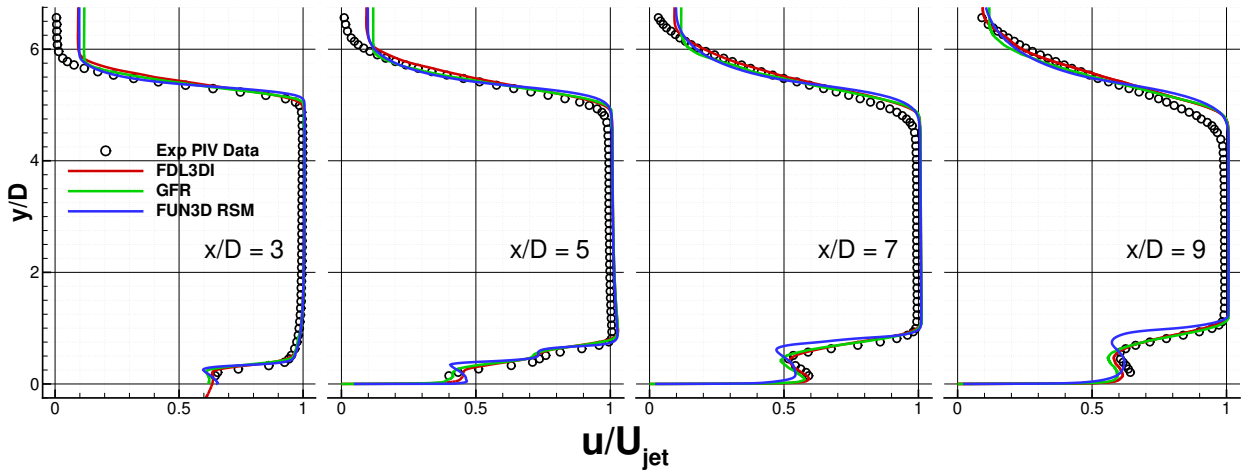

(a) Mean streamwise velocity profiles for BR = 1.0.

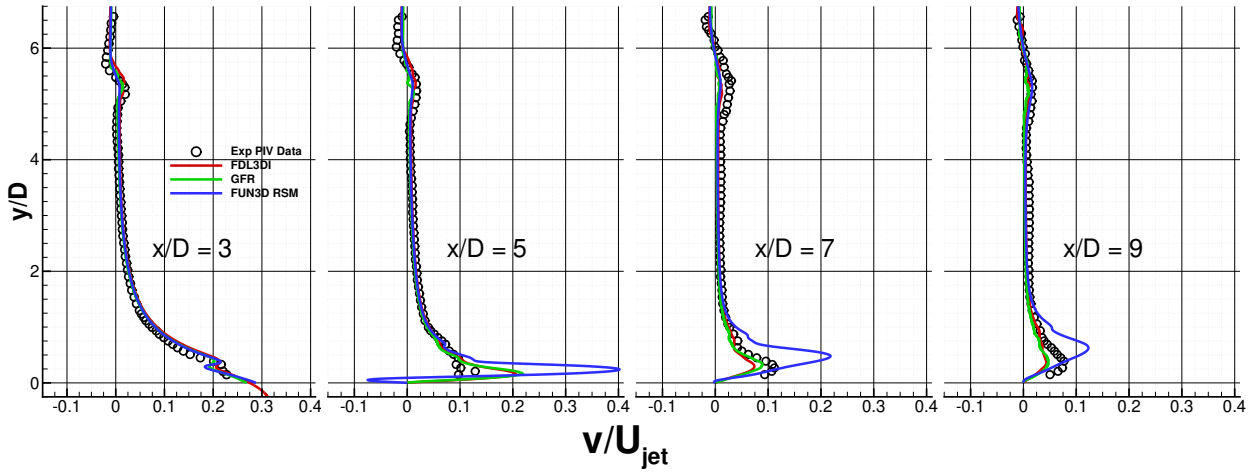

(b) Mean vertical velocity profiles for BR = 1.0.

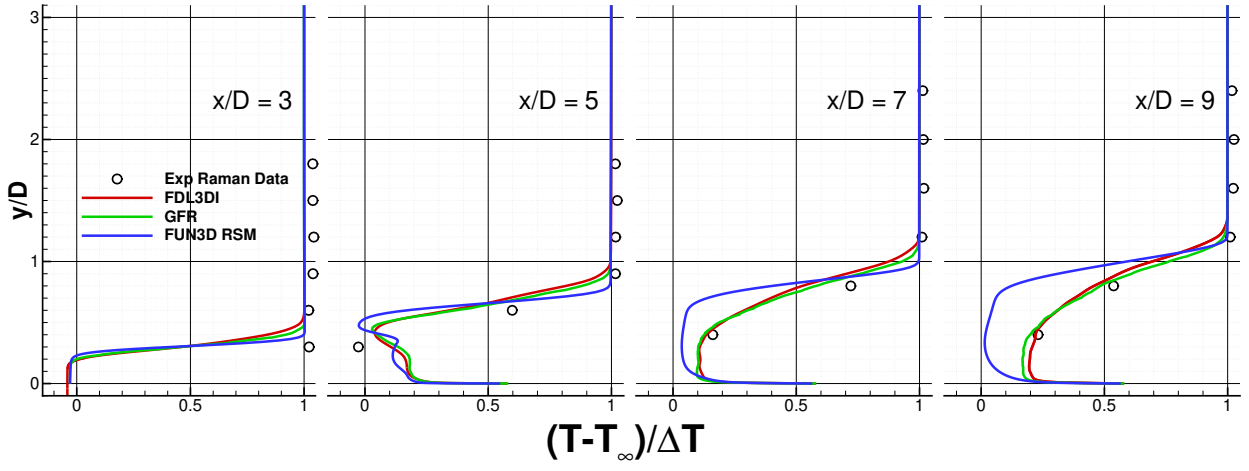

(c) Mean temperature profiles for BR = 1.0.

Figure 8: Comparison between experiment, LES from FDL3DI, LES from GFR, and RANS from FUN3D of 1D profiles of mean variables taken at various axial locations along the plate centerline for BR = 1.0.

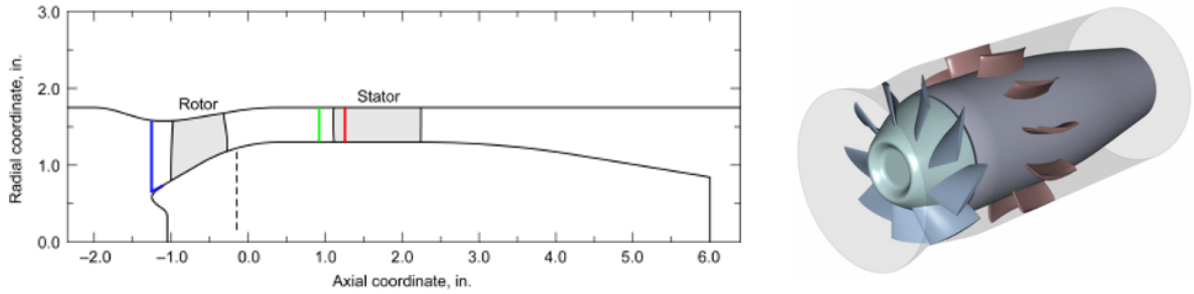

(a) Meridional view

(b) Three-dimensional view

Figure 9: Spacecraft cabin ventilation fan geometry. In the meridional view, the color lines represent the GFR domain extents. The blue line represents the location of the inflow boundary and slight modification to the hub leading edge, the green line is the axial location for the start of the sponge region, and the red line is the end of the sponge region and outflow boundary. Note, the sponge region does not include the stator blade.

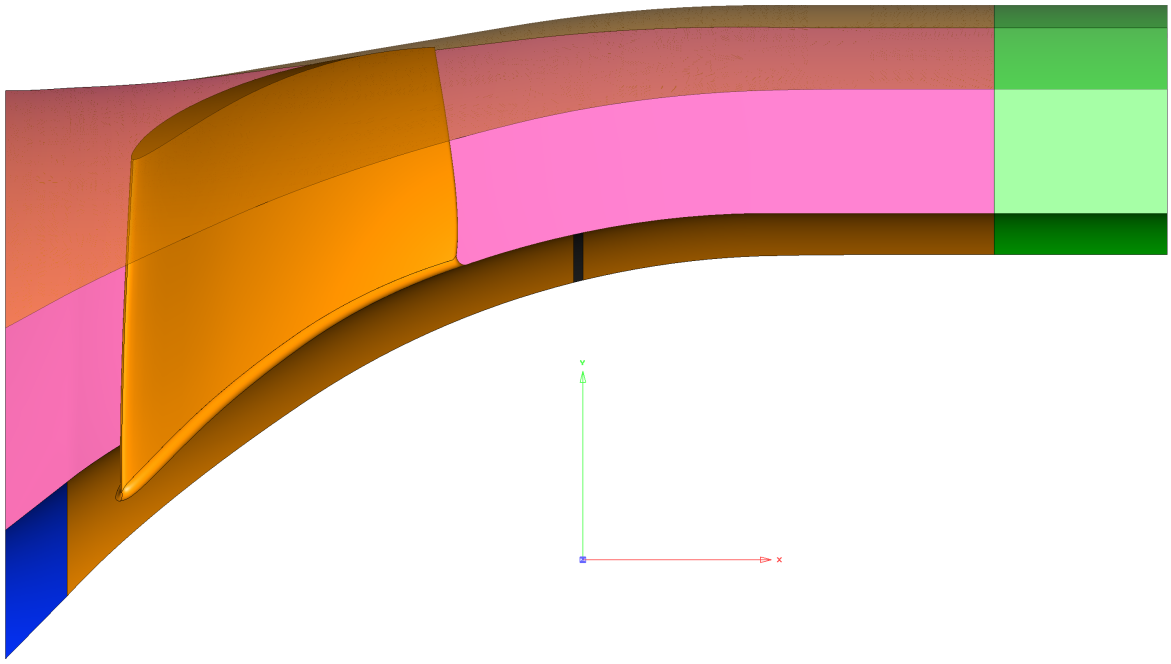

Figure 10: Geometry of the domain used for GFR simulations of the spacecraft cabin ventilation fan. The sponge region added on to the outflow boundary is the green section on the right. The blue region is the part of the hub domain that has been modified from the physical geometry to facilitate a more stable inflow. The thin black surface behind the blade is the physical air gap between the rotating and stationary parts of the hub which has been filled in with a wall boundary for these simulations.

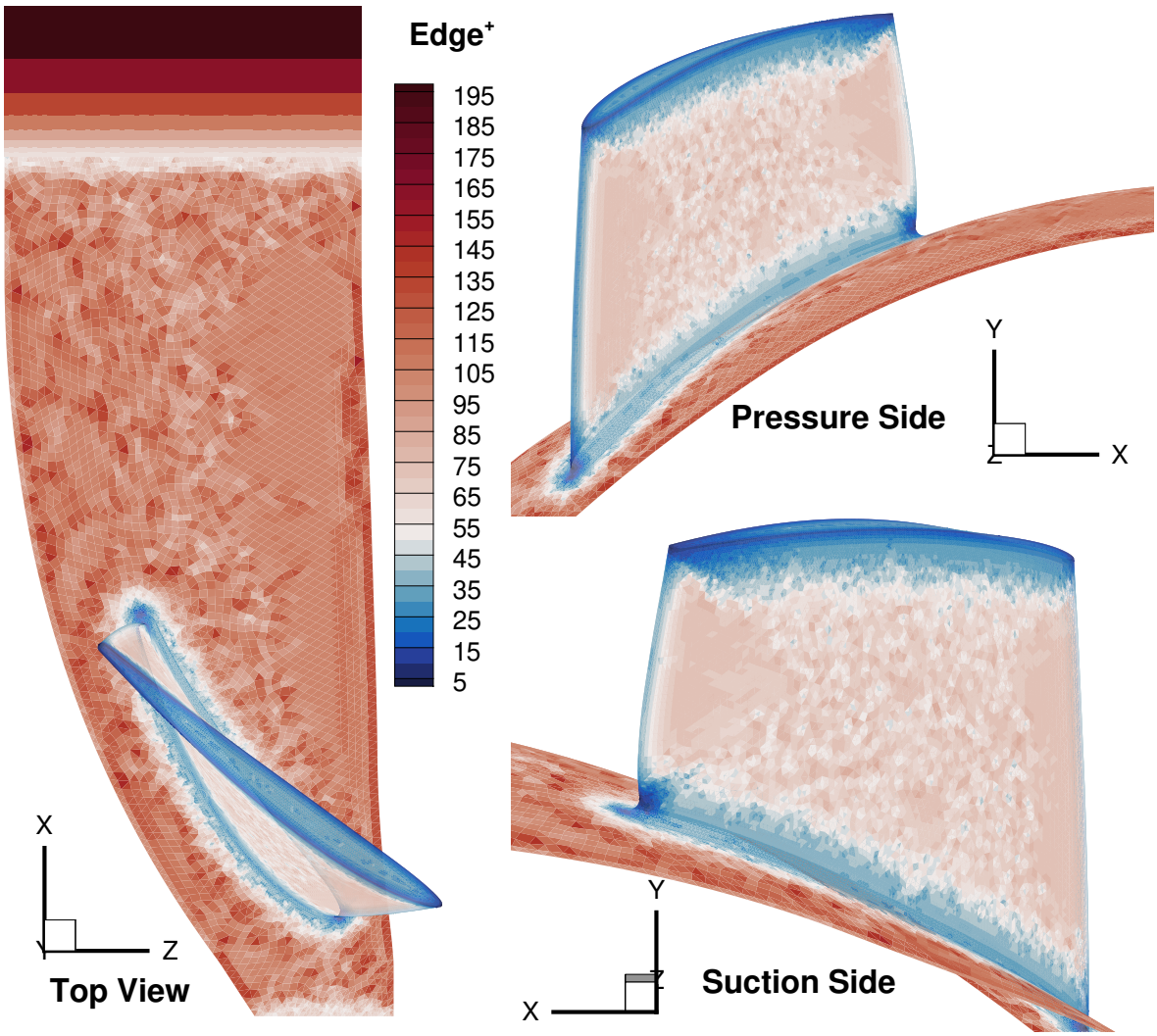

Figure 11: Contours of the edge length in wall units for the rotor and hub surface meshes. For quadrilateral surface elements, the edge length, l, is computed as $l = \sqrt{A}$, where A is the area of the element. The edge length for triangle surface elements is based on an equilateral triangle assumption where $l = \sqrt{4A/\sqrt{3}}$. Note that the wall unit spacing based on the DoF is found by computing $\text{edge}^+/(\mathcal{P}+1)$, where $\mathcal{P}$ is the degree of the solution polynomial used for the simulation.

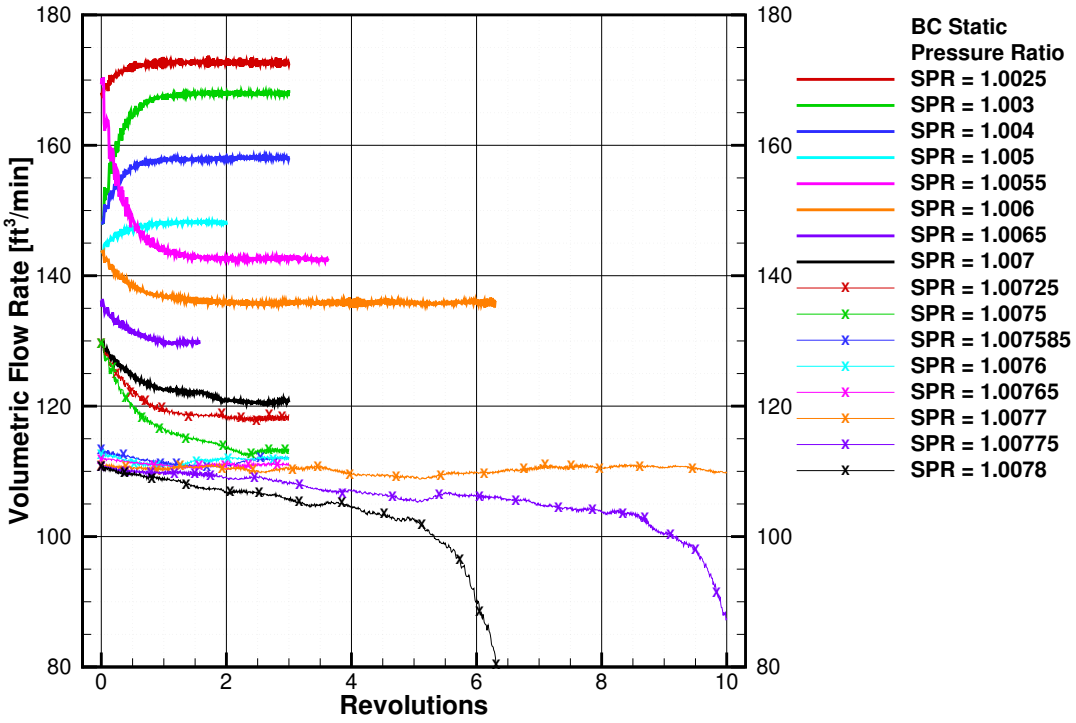

(a) Volumetric flow rate

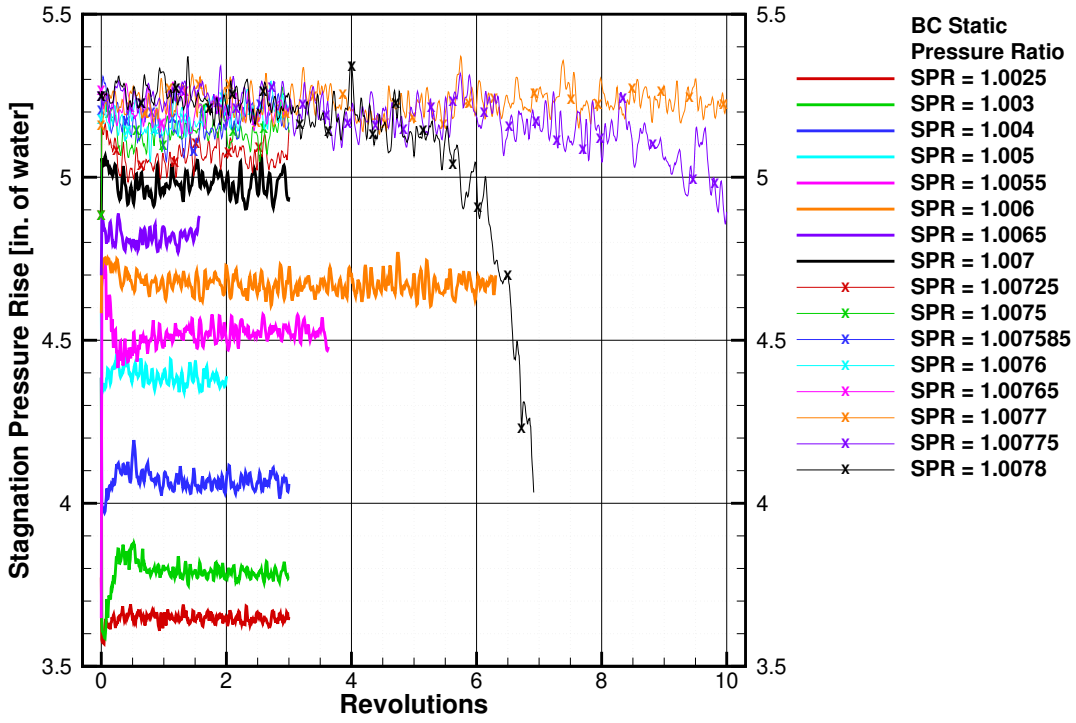

(b) Stagnation pressure rise

Figure 12: Convergence of the boundary conditions for each of the operating points run at $\mathcal{P}1$ used to create the fan performance map. Each plot shows the time history of integrated boundary quantities versus the number of full revolutions completed by each simulation.

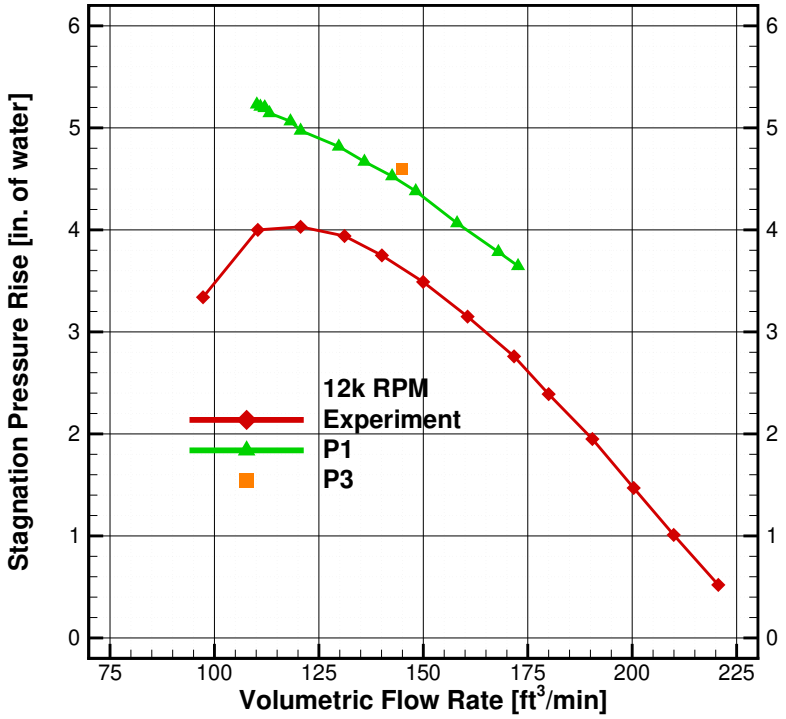

(a) Stagnation pressure rise vs volumetric flow rate compared to experiment.

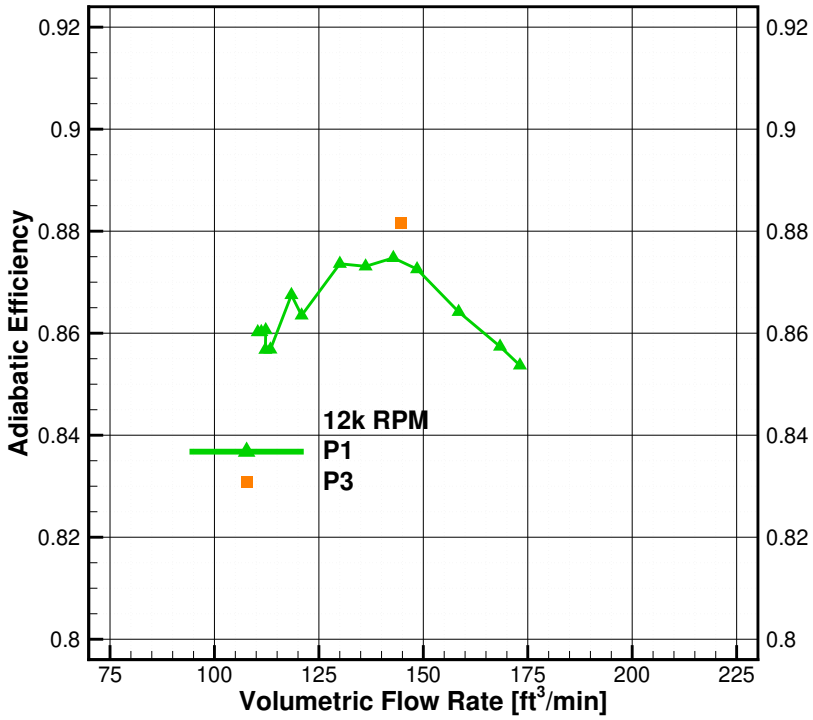

(b) Adiabatic efficiency vs volumetric flow rate.

Figure 13: Fan performance maps at 12,000 RPM obtained from all of the $\mathcal{P}1$ simulations that did not stall. Both plots also contain the single $\mathcal{P}3$ case that was run long enough to reach a converged volumetric flow rate.

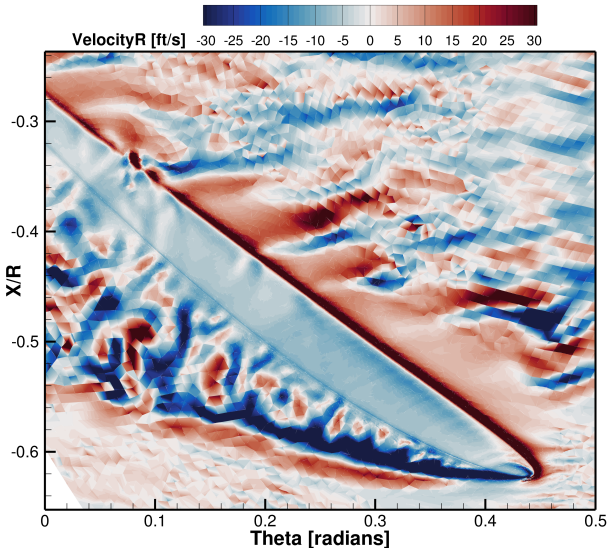

(a) $\mathcal{P}1$ solution with 12.9 million DoF.

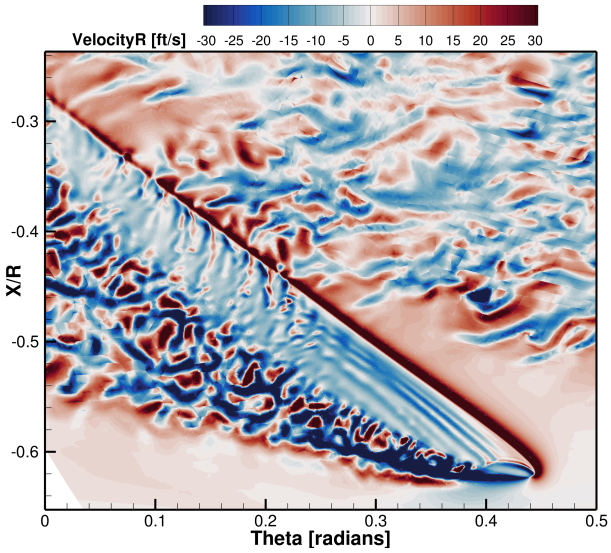

(b) $\mathcal{P}2$ solution with 38 million DoF.

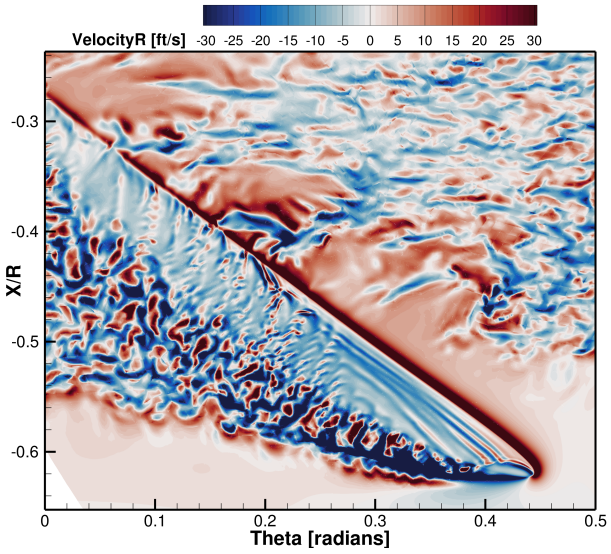

(c) $\mathcal{P}3$ solution with 84 million DoF.

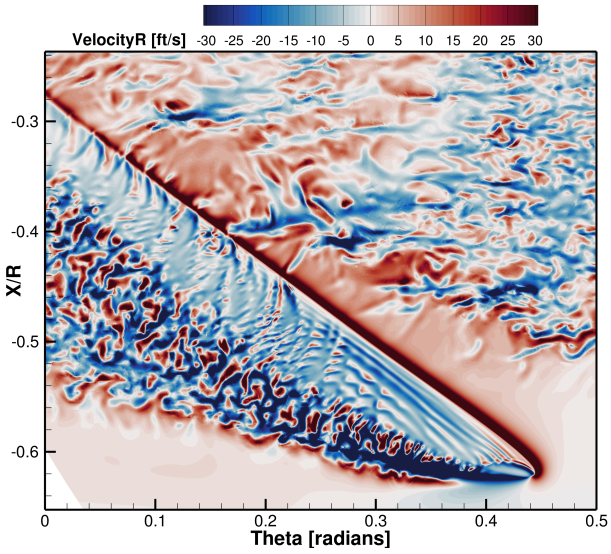

(d) $\mathcal{P}4$ solution with 157 million DoF.

Figure 14: Instantaneous contours of radial velocity shown along an isosurface of 99% passage height, which places the surface within the gap between the tip of the rotor blade and the case. The view is looking through the case with the tip of the rotor blade hidden behind the contours. The freestream flow is from the bottom to the top of each image, with the blades rotating left to right. All four simulations were started from the same established $\mathcal{P}1$ solution, and these contours were all taken after 0.2522 revolutions had passed.

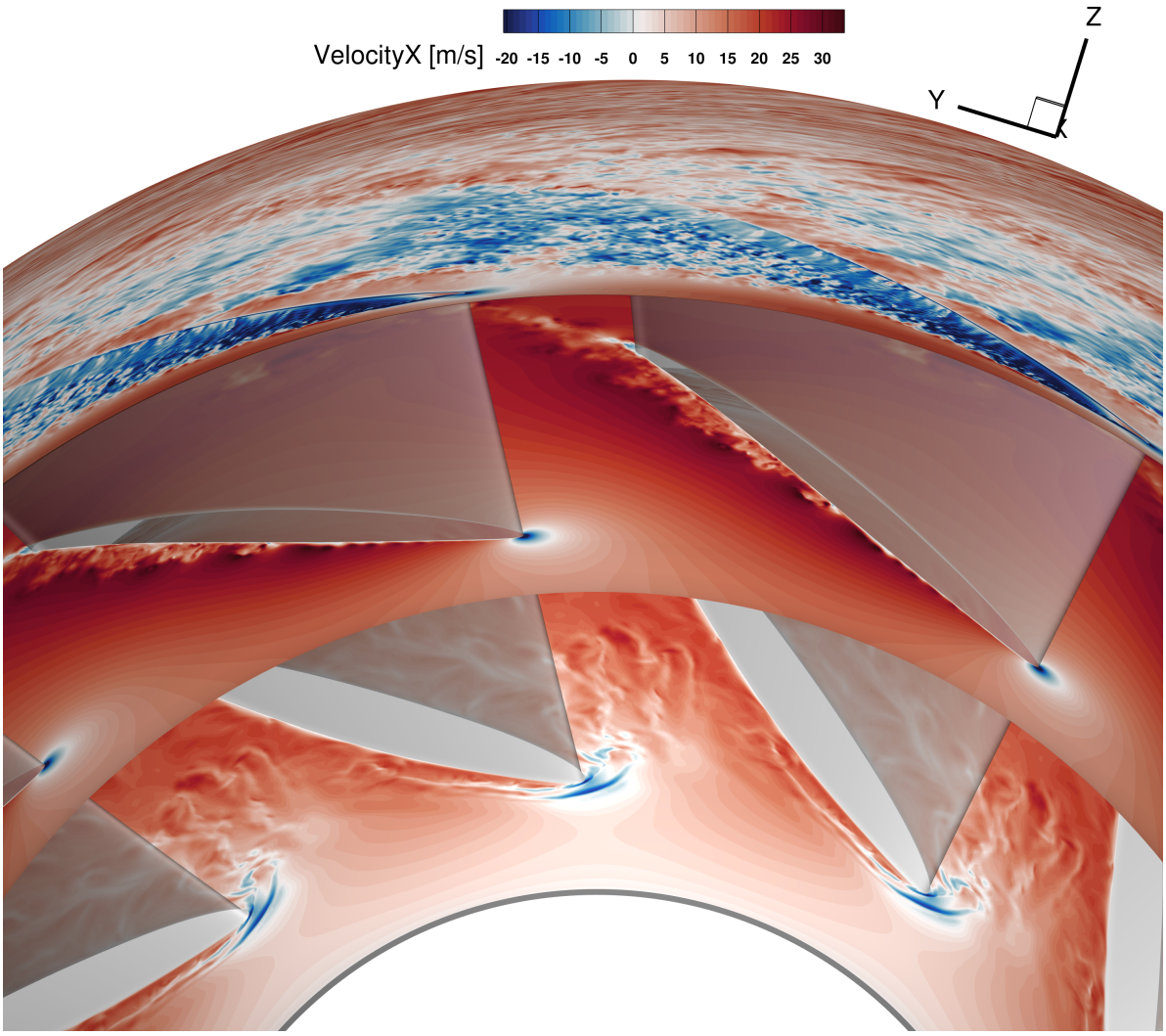

Figure 15: Instantaneous contours of axial velocity along isosurfaces of 1%, 50%, and 99% passage height. This freestream flow is going into the page, and the translucent rotor blades are rotating clockwise from this point of view.